iScience

CellPress

Article

Ultrathin Nanosheet of Graphdiyne-Supported Palladium Atom Catalyst for Efficient Hydrogen Production

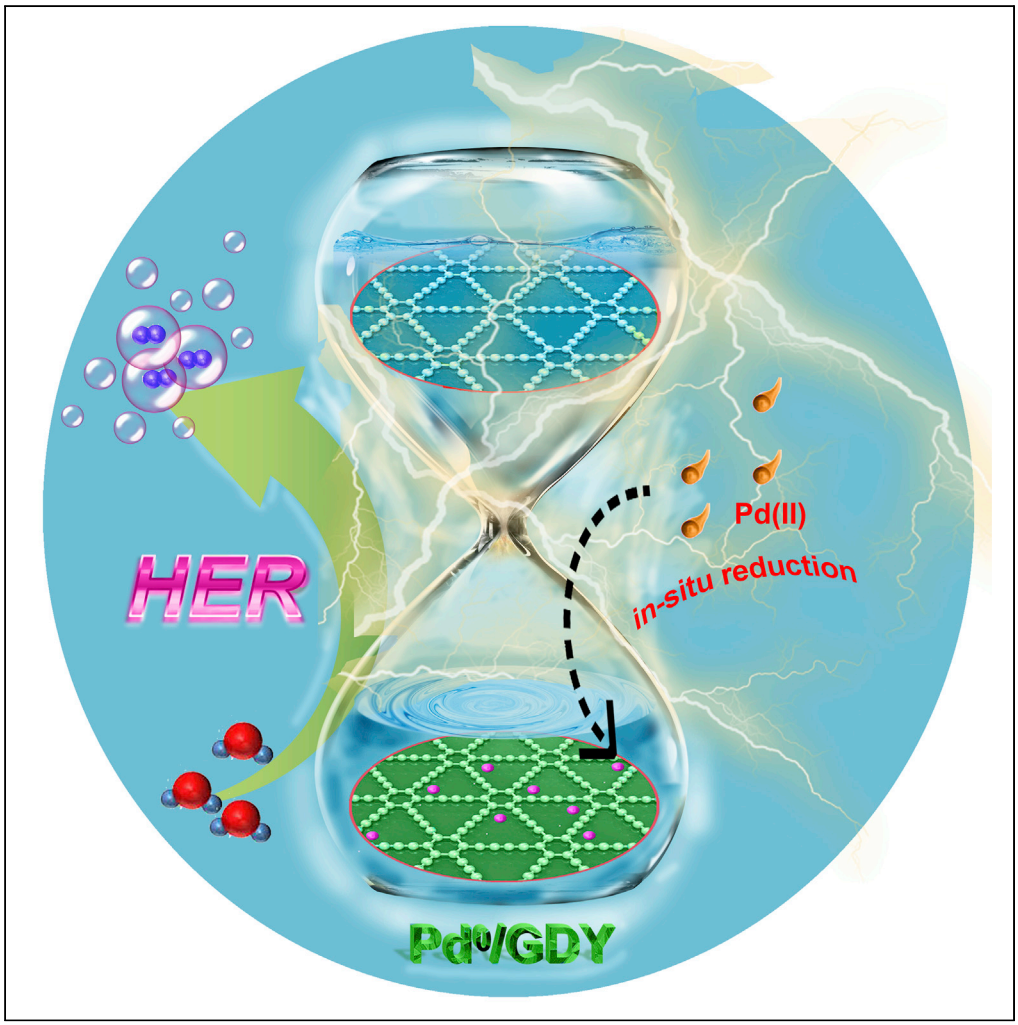

Huidi Yu, Yurui Xue, Bolong Huang, ..., Yongjun Li, Huibiao Liu, Yuliang Li

xueyurui@iccas.ac.cn (Y.X.)
bhuang@polyu.edu.hk (B.H.)
ylli@iccas.ac.cn (Y.L.)

HIGHLIGHTS

A general approach for synthesis of zero-valent palladium atoms on graphdiyne

Pd atoms anchored at the angle site of the alkyne ring in GDY

The obtained atomic catalyst shows better catalytic activity than commercial Pt/C

The unique structure maintains and guarantees efficient HER process

Yu et al., iScience *11*, 31–41
January 25, 2019
https://doi.org/10.1016/j.isci.2018.12.006

iScience

CellPress

Article

Ultrathin Nanosheet of Graphdiyne-Supported Palladium Atom Catalyst for Efficient Hydrogen Production

Huidi Yu,[1] Yurui Xue,[1,*] Bolong Huang,[2,*] Lan Hui,[1] Chao Zhang,[1] Yan Fang,[1] Yuxin Liu,[1] Yingjie Zhao,[3] Yongjun Li,[1] Huibiao Liu,[1] and Yuliang Li[1,3,4,5,*]

SUMMARY

Atomic catalysts are promising alternatives to bulk catalysts for the hydrogen evolution reaction (HER), because of their high atomic efficiencies, catalytic activities, and selectivities. Here, we report the ultrathin nanosheet of graphdiyne (GDY)-supported zero-valent palladium atoms and its direct application as a three-dimensional flexible hydrogen-evolving cathode. Our theoretical and experimental findings verified the successful anchoring of Pd^0 to GDY and the excellent catalytic performance of Pd^0/GDY. At a very low mass loading (0.2%: 1/100 of the 20 wt % Pt/C), Pd^0/GDY required only 55 mV to reach 10 mA cm^{-2} (smaller than 20 wt % Pt/C); it showed larger mass activity (61.5 A mg_{metal}^{-1}) and turnover frequency (16.7 s^{-1}) than 20 wt % Pt/C and long-term stability during 72 hr of continuous electrolysis. The unusual electrocatalytic properties of Pd^0/GDY originate from its unique and precise structure and valence state, resulting in reliable performance as an HER catalyst.

INTRODUCTION

Electrochemically splitting water into hydrogen (H_2) through the hydrogen evolution reaction (HER) is a promising strategy for solving the problems of energy scarcity and environmental pollution (Goff et al., 2009; Jiao et al., 2015; Liu et al., 2018; Roger et al., 2017; Walter et al., 2010; Yang et al., 2018). In general, platinum (Pt)-based materials are at present the most efficient electrocatalysts for the HER process, but the high cost and natural scarcity of Pt remain great obstacles limiting their practical use. There is, therefore, a quest to develop alternative electrocatalysts—displaying high activity and stability at low cost—for water splitting. Much effort has been devoted recently to the development of non-precious HER electrocatalysts, including those based on transition metals (e.g., Fe, Co, Ni, Mo) (Karunadasa et al., 2012; Luo et al., 2014, 2018; Zou et al., 2014) and those that are metal free (e.g., graphene, carbon nanotubes [CNTs], C_3N_4) (Dai et al., 2015; Jiao et al., 2015; Liu et al., 2015, 2016). Although these electrocatalysts have potential as alternatives to Pt-based ones, their relatively low HER activities do not yet meet the needs of real applications. Atomic catalysts (ACs), consisting of single metal atoms anchored on supporting materials, can expose the maximum number of active sites, maximize the atom utilization efficiency and reaction selectivity, and boost a system's electrocatalytic activity (Fei et al., 2018; Jones et al., 2016; Liu et al., 2016; Thomas, 2015;Xue et al., 2018a, 2018b). These features suggest an optimal strategy for synthesizing cost-effective and active catalysts, especially for those based on noble metals (e.g., Ir, Au, Pt) (Jones et al., 2016; Liu et al., 2016). The high surface energies of single metal atoms can, however, encourage aggregation during preparation and catalysis processes, decreasing the number of active sites and limiting the catalytic efficiency and stability. An appropriate support that can anchor single metal atoms firmly, to avoid their aggregation, is necessary when synthesizing active and stable ACs. Single metal atoms anchored onto various metals, metal oxides (Li et al., 2014a, 2014b; Nie et al., 2017; Wang et al., 2013), and carbon materials (e.g., graphene, graphite carbon, other carbon materials having N_4C_4 moieties) (Chen et al., 2017; Fan et al., 2016; Fei et al., 2018; Yin et al., 2016) have previously been preferred in the development of ACs. Their catalytic applications have, however, been greatly hindered by several major disadvantages. For example, their syntheses can be very rigorous, complex, hard to manage, and incapable of avoiding metal clusters/particles, potentially resulting in uncertain structures for the supports, the metal sites, and the active sites, diminishing the catalytic performance. Furthermore, their low conductivity, low loading density, and poor stability/tolerance can also restrict the catalytic efficiency of the ACs. These limitations make it difficult to unambiguously identify the real active sites or obtain an atomic-level understanding of the relationship

[1]Key Laboratory of Organic Solids, Institute of Chemistry, Chinese Academy of Sciences, Beijing 100190, PR China

[2]Department of Applied Biology and Chemical Technology, The Hong Kong Polytechnic University, Hung Hom, Kowloon, Hong Kong SAR, China

[3]School of Polymer Science and Engineering, Qingdao University of Science and Technology, Qingdao 266042, P.R. China

[4]University of Chinese Academy of Sciences, Beijing 100049, PR China

[5]Lead Contact

*Correspondence: xueyurui@iccas.ac.cn (Y.X.), bhuang@polyu.edu.hk (B.H.), ylli@iccas.ac.cn (Y.L.)

https://doi.org/10.1016/j.isci.2018.12.006

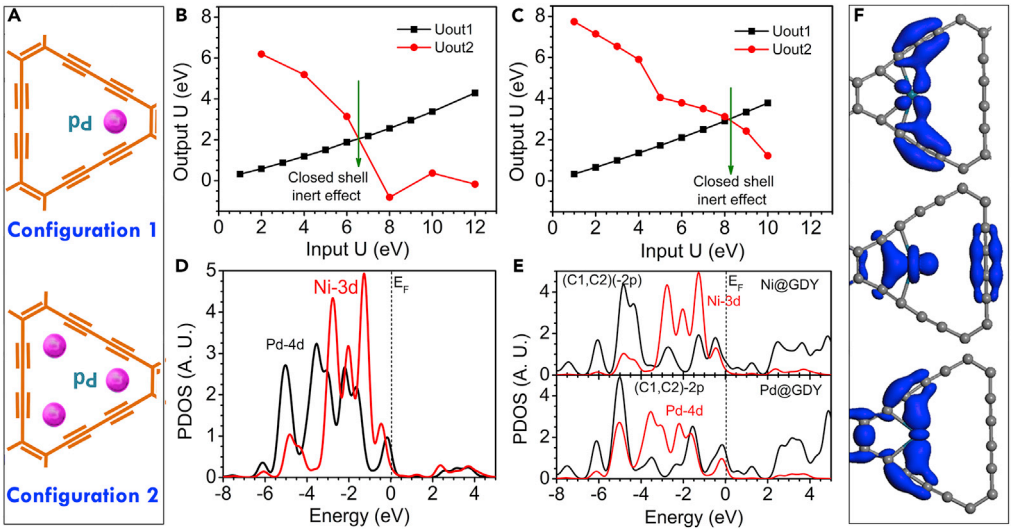

Figure 1. Optimized Configurations of Pd^0/GDY

(A) The energetically favored singly (higher) and triply (lower) anchoring sites (A-site) for Pd within the GD system.

(B and C) The orbital potential energy projections (U_{out1} and U_{out2}) for Pd 4d within (B) singly and (C) triply anchoring site.

(D) The PDOS comparison for the Pd 4d and Ni 4d bands within GD-Pd and GD-Ni, respectively.

(E) The PDOSs for overall contribution of the Pd 4d and (C1, C2) 2p band comparing with Ni 4d and (C1, C2) 2p band.

(F) The real-space 3D orbital contour plot for the three dominant p–d band overlapping peaks observed from the PDOS between Pd 4d and (C1, C2) 2p bands.

between the structures and catalytic properties. Moreover, all the previously reported traditional ACs have had undetermined valence states or values that are not integers. Although scientists have for some time been predicting the emergence of zero-valent metal single-atom catalysts, the preparation of zero-valent ACs has remained challenging in the field of catalysis, with the goal of a reasonable design for new-generation ACs with controllable structures and high catalytic performances.

Graphdiyne (GDY), a relatively new two-dimensional (2D) planar carbon allotrope comprising sp^2-hybridized carbon atoms in benzene rings linked through sp-hybridized carbon atoms in diacetylenic groups has attracted great attention in chemistry, physics, and material science ever since its first successful synthesis by our group (Huang et al., 2018; Jia et al., 2017; Li, 2017; Li et al., 2010, 2014a, 2014b; Matsuoka et al., 2017; Xue et al., 2018a, 2018b; Yu et al., 2018). In particular, it has been proposed as an excellent substrate for anchoring zero-valent metal atoms (Xue et al., 2018a, 2018b). The sp-hybridized carbon atoms endow GDY with many attractive properties, including a natural band gap, high electric conductivity, high charge carrier mobility, excellent chemical/mechanical stability, and uniformly distributed pores (Long et al., 2011). In contrast to other conventional carbon materials (e.g., graphene, CNTs), the coexistence of sp (p_x–p_y π/π^* states) and sp^2 (p_z π/π^* state) hybridization in GDY means that the π/π^* orbitals can rotate in any direction perpendicular to the −C≡C− bonds (He et al., 2012). This feature is favorable for chelating single metal atoms and greatly contributed to strong charge transfer between the metal atoms and the GDY. Our theoretical investigations have revealed that the most favorable adsorption site for single metal atoms on GDY is at the angle site (A-site) of the alkyne ring (Figures 1B and 1C). The unique properties of GDY suggest that it has tremendous potential for the fabrication of active and stable ACs.

Zero-valent palladium (Pd^0) complexes are the active species in many catalytic transformations, including Pd-catalyzed Heck and cross-coupling reactions (Kolter et al., 2017;Zheng et al., 2014). To the best of our knowledge, however, no previous reports have described the HER catalyzed by single Pd^0 catalysts or the correlations between the active site structure and the HER activity at the atomic level.

Inspired and motivated by all facts mentioned above, in this study we demonstrated such a zero-valent electrocatalyst system consisting of Pd^0 anchored on GDY for significant improvement in HER performance. Both theoretical and experimental findings revealed the successful anchoring of the single zero-valent Pd^0 atoms to the GDY. The Pd^0/GDY samples exhibited outstanding electrocatalytic activity, with an

overpotential of 55 mV at 10 mA cm^{-2}, a mass activity of 61.5 A mg_{metal}^{-1}, and a turnover frequency of 16.7 s^{-1}, which are better than those of 20% Pt/C. This excellent HER performance originated from the unique and well-defined chemical and electronic structures of Pd^0/GDY.

RESULTS

Theoretical Evaluation

We examined the key mechanism behind the excellent HER performance of the Pd-GDY system (see also Transparent Methods). We tested the locations of the Pd atoms within the Pd-GDY system in two cases: one in which a Pd atom was singly anchored at the A-site (Figure 1A) and the other in which it was triply anchored at the A-site (Figure 1B). Using our previously developed two-way crossover linear response method, we decomposed the response of the electronic potential of an on-site targeted orbital (Huang., 2016a, 2016b, 2016c, 2017). The characteristics of the Pd 4d orbital at the A-site are illustrated, regarding the two different anchoring modes. We observed a variation in the character of the Pd 4d orbital, displaying a closed shell (crossover) effect for both the singly and triply symmetrically anchored Pd atoms at the A-site (Figures 1C and 1D). This crossover effect is indicative of strong orbital overlaps between the Pd atom and the neighboring C atoms, namely, coupled long-range coupling (p–d) between Pd 4d orbitals and the C1 and C2 2p orbitals; here, C1 and C2 denote the nearest neighboring and second nearest neighboring C atoms with respect to the Pd anchoring position. The orbital energy also increased from 6.55 to 8.21 eV. This observation implies that the electronegativity was enhanced as a result of the potential for d–d orbital resonant coupling by the nearby Pd atom in the case of triple anchoring. Moreover, it suggests a strong tendency for zero-valent anchoring of Pd^0 within the GDY system.

We further compared the electronic properties with those we had determined previously for Ni^0 anchoring (Xue et al., 2018a, 2018b). The projected partial density of states (PDOSs) illustrated the Pd 4d and Ni 3d bands (Figure 1D). Moreover, the relatively deeper 4d band center would activate more 4d electrons from the Pd site onto the nearby bonded C1 and C2 sites. In more detail, Figure 1E illustrates the PDOS of the C1 and C2 2p orbitals combined with the d bands of Pd and Ni, respectively. We find that the deeper d band center of the anchoring Pd atom may have arisen from the strong p–d coupling. The 2p band exhibited greater matching with the Pd 4d band distribution when compared with that of the Ni-GDY system. Nevertheless, the Ni 3d band localized in the higher range exhibited less of a p–d band matching effect with the C 2p band. Therefore, the bonding between the Pd atom and the C1 and C2 sites was stronger than that in the corresponding Ni-GDY system, resulting in substantial charge transfer between the Pd atom and the nearby C sites. On the other hand, the electronic activities for the catalytic HER within Pd-GDY can be determined by the Pd-(C1, C2) entity, where the p–d coupled band center is almost dominated by the Pd 4d orbital (Figure 1E). The localized orbitals of the valence electronic states are presented in terms of a real-space contour plot. The localized states represent the three dominant peaks of the Pd 4d band strongly overlapping with the (C1, C2)-2p band. These orbitals reveal that the anchoring Pd site and the nearby (C1, C2) site can mutually transfer their electrons between the 4d and 2p orbitals, even through a long-range interaction (Figure 1F).

Next, we examined the energetic activities to elucidate the HER mechanism (see also Transparent Methods). We considered both the H/2H formation energies and the related H-chemisorption energies (Figure 2A). The various C active sites are labeled C1–C4 (Figure 2B). We found that the C sites positioned closer to the anchoring Pd atom exhibited an energetically favorable adsorption trend for H; for 2H, the adsorption trend was similar. Regarding the strong coupling between the Pd and (C1, C2) sites, as well as the optimal p–d band matching effect, we confirmed that the adsorption energy of the C1 and C2 sites was lower than that of the C3 site. In addition, we verified that the C2 site was the most active site, displaying a strong energetic preference to adsorb the H atom. From the viewpoint of chemisorption, the C3 and C4 atoms were preferred as H desorption centers, because their energy levels remained above the thermoneutral line (ΔG = 0 eV). Nevertheless, we confirmed that the C1 and C2 sites had a promoting effect for the stable adsorbing of the H atom, with less of an over-binding effect when compared with the Ni-GDY system (Xue et al., 2018a, 2018b). This trend arose because the C1 and C2 sites both exhibited an optimal band matching effect. It further implies that strong p–d charge transfer occurred to activate the d electrons from the Pd atom onto the C1 and C2 sites for H atom adsorption (Figure 2C). Thus the chemisorption energies are consistent with the discussion above regarding the electronic properties. Taken together, these results imply the great potential of Pd^0/GDY for catalytically efficient hydrogen evolution.

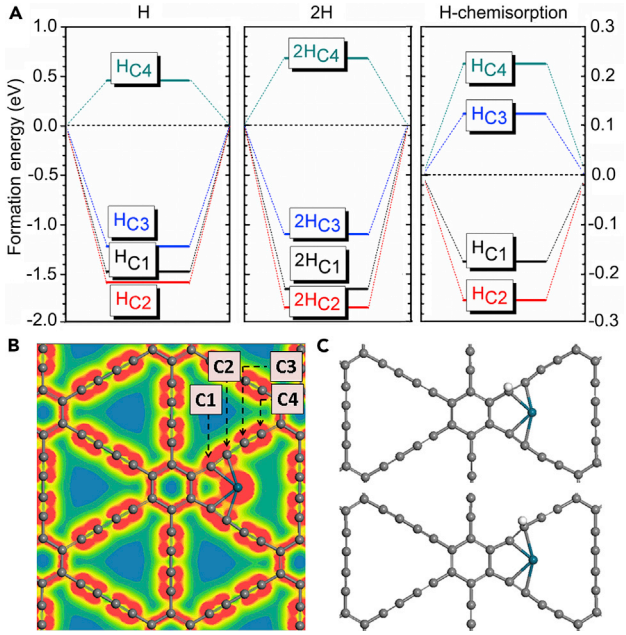

Figure 2. Adsorption Formation Energies and Corresponding Structural Configurations

(A) Adsorption formation energies of H and 2H on four different C atom sites (C1, C2, C3, C4) nearby the anchoring Pd atom. The free chemisorption energies are also given.

(B) 2D Valence charge density mapping with the four different C atom sites given (C1, C2, C3, C4).

(C) Structural configuration for H atom adsorption on the C1 and C2 atom sites.

Morphological Characterization

To substantiate the predictions from density functional theory experimentally, we synthesized Pd^0/GDY through a facile synthetic method (please see Transparent Methods for details). Inductively coupled plasma mass spectrometry revealed that the Pd loading was 0.2 wt %. As shown in Figures 3A–3D, a film of vertically aligned and interlaced GDY nanosheets (ca. 200 nm in size) was grown on a smooth interweaved CF surface (Figure S1) through Glaser-Hay coupling using hexaethynylbenzene as the precursor, forming a 3D GDY foam (Gao et al., 2017; Zhou et al., 2015). The morphology of GDY was confirmed using scanning electron microscopy (Figures 3A, 3B, and S2) and transmission electron microscopy (TEM; Figures 3C, 3D, and S3). Then the ultrathin nanosheet of GDY-supported palladium atom catalyst was obtained (Figures 3E–3H, S4, and S5). Both scanning electron microscopy and TEM indicated that the nanosheet morphology was preserved after the synthesis of Pd^0/GDY (Figures 3E–3H), confirming the robust nature of GDY skeleton—a useful feature for improved catalysts. High-resolution TEM revealed that the Pd^0/GDY nanosheet had an interplanar distance of 0.329 nm (Figure 3H), smaller than that of the pure GDY nanosheet (0.365 nm, Figure 3D). The smaller spacing between the two adjacent GDY layers implies an associated interaction between the GDY and the Pd atoms. Moreover, no Pd clusters/particles were evident in the scanning electron microscopic and TEM images, suggesting that the anchored Pd atoms were not in aggregated form, unlike those in the reference sample (Figure S6; see also Transparent Methods). Scanning TEM (STEM) (Figure 3I) and corresponding elemental mapping images (Figures 3J–3L) show the uniform distribution of C and Pd elements over the nanosheets. In addition, contact angle measurement results reveal that, after the growth of the GDY, the hydrophobic surface of bare CF (contact angle: 140.5°; Figure 3M) becomes completely wetting (contact angle: 0°; Figure 3N), which could significantly improve the wetting between the electrode and electrolytes, therefore finally reducing the ohm contact resistance and benefiting the enhancement of catalytic performances.

Atomic Structure and Chemical State Analysis

We employed sub-ångström-resolution, aberration-corrected high-angle annular dark-field (HAADF) STEM to collect information about the configuration and dispersion of the individual Pd atoms on the

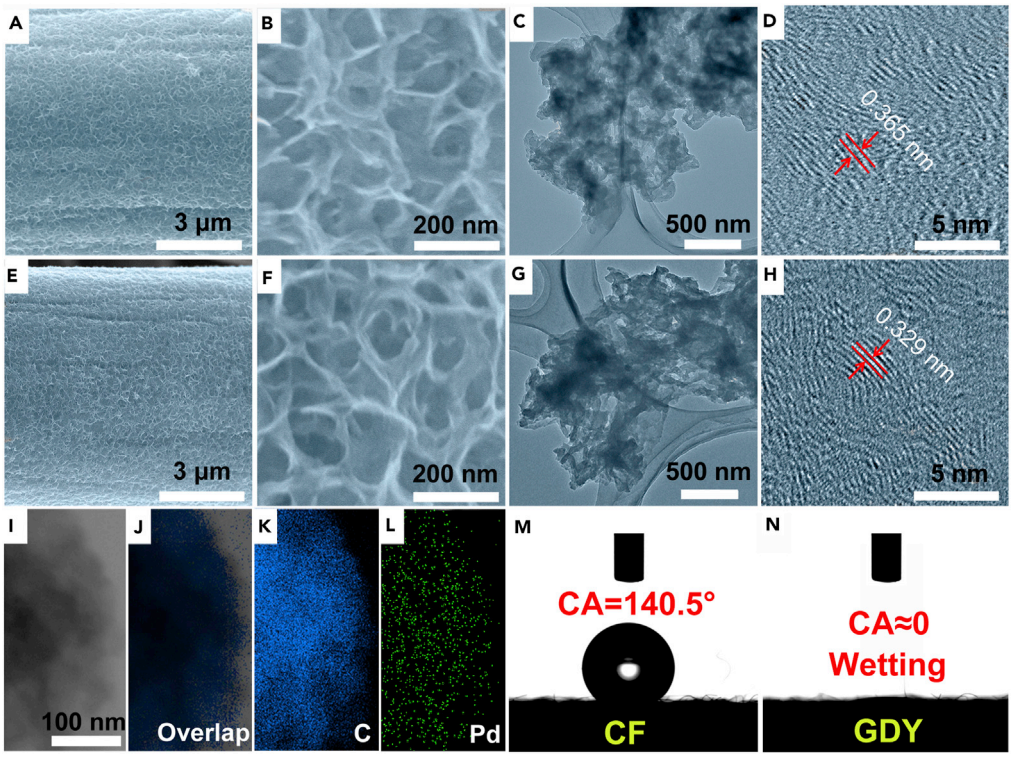

Figure 3. Morphological Characterization of Samples

(A-H) (A and B) SEM, (C) TEM and (D) HRTEM images of pristine GDY, see also Figure S2 and S3; (E and F) SEM, (G) TEM and (H) HRTEM images of Pd^0/GDY, see also Figure S4 and S5.

(I–L) STEM (I) and elemental mapping (J–L) images of Pd^0/GDY.

(M and N) Contact angle measurements on pure CF (M) and GDY (N).

GDY (Ortalan et al., 2010). The HAADF images of Pd^0/GDY nanosheets recorded from different batches of samples revealed the separate and uniform distribution of the individual Pd atoms (white dots) on the GDY, without any aggregation (Figures 4A–4L). STEM images and corresponding elemental mapping analysis (Figures 4M–4P) clearly indicated the atomic and homogeneous dispersion of the Pd atoms in the Pd-GDY nanosheets, in accordance with the above-mentioned TEM- energy dispersive X-ray analysis (EDX) data (Figures 3I and 3J).

We also performed elemental selective X-ray absorption fine structure spectroscopy, including extended X-ray absorption fine structure (EXAFS, Figure 5A) and X-ray absorption near-edge structure (XANES) spectroscopy (Figure 5B). The EXAFS spectrum of Pd-GDY featured a major peak near 1.5 Å, which is smaller than that of the Pd–Pd contribution (ca. 2.5 Å) in Pd foil, reflecting the existence of only singly dispersed Pd atoms in Pd-GDY. No diffraction peaks corresponding to Pd nanoparticles (Pd NPs) were evident in the X-ray diffraction pattern of Pd^0/GDY (Figure S7A), further implying the absence of Pd NPs. The first derivative of the XANES is generally used as the basis for energy calibration and used to determine the valence states of samples (Xue et al., 2018a, 2018b). As shown in Figure 5B, the main peaks of Pd/GDY and Pd foil are located at the same energies, providing evidence that zero-valence Pd atoms are anchored on GDY. Clearly, the anchoring of the single metal atoms on the GDY was universal and reproducible; they had not merely coincidentally emerged within a confined region. These results provided sufficient proof for the successful preparation of the Pd-GDY AC. Through careful analysis of the recorded HAADF images, we obtained the average diameter of the individual Pd atoms anchored on the GDY (Figure S8) within a very narrow size distribution: 3.6 $\pm$ 0.1 Å, consistent with the typical size of a Pd atom (3.6 Å).

Raman spectroscopy (Figures 5C and S9) revealed that the peaks corresponding to the vibration of the conjugated diyne units of the Pd^0/GDY samples shifted to higher wave number compared with those of

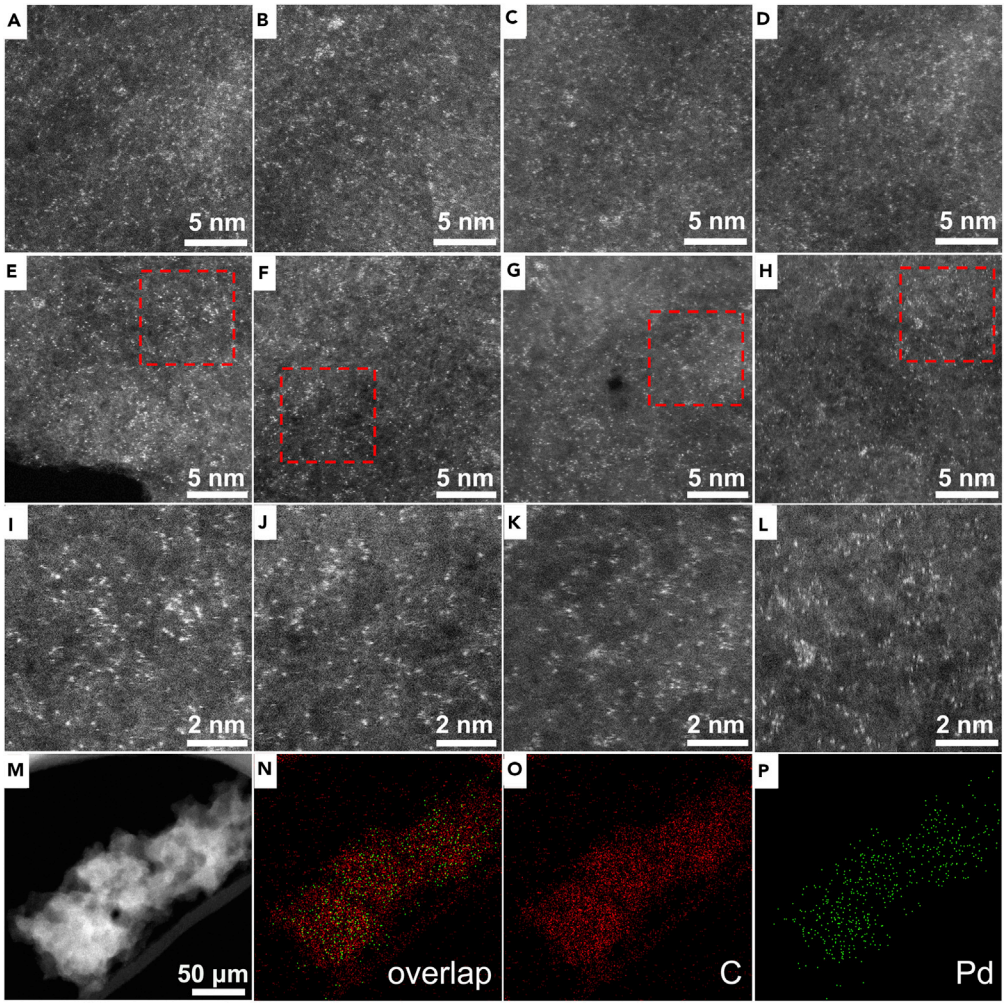

Figure 4. Atomic Resolution Images of HAADF-STEM Pd^0/GDY

(A–H) HAADF images obtained from various regions of Pd^0/GDY nanosheets.

(I–L) Enlarged images of the selected regions in (E–H).

(M–P) STEM-HAADF image of the Pd^0/GDY nanosheet and corresponding elemental mappings of Pd and C atoms.

the pristine GDY—the result of the anchoring of the Pd atoms. The D band to G band ratio for Pd^0/GDY (0.80) is larger than that for pristine GDF (0.75), which indicates that the Pd^0/GDY structure is much more defective than GDY, leading to more active sites for efficient catalysis. We used X-ray photoelectron spectroscopy (XPS) to examine the chemical states of the Pd atoms. The survey spectrum (Figure 5D) revealed the presence of Pd and C elements in Pd^0/GDY, whereas only C elements were evident in the GDY sample. Figure 5E presents the high-resolution C 1s XPS spectra of the samples. The spectrum of Pd^0-GDY exhibited a new peak at 290.8 eV, due to the π–π^* transitions arising from restoration of the delocalized conjugated structure (Figure S7B), suggesting the presence of interactions between the Pd atoms and the GDY (Xue et al., 2018a, 2018b; Yu et al., 2018). The area ratio of the sp^2-C and sp-C peaks remained at 2:1, reflecting the integrity of the GDY structure after the anchoring of the Pd atoms. All these findings are persuasive for an intimate interaction between the anchored individual Pd atoms and the GDY, arising from the unique electronic and chemical structures of the GDY. The high-resolution XPS spectrum of the Pd 3d orbitals (Figure 5F) featured the peaks of Pd $3d_{5/2}$ and Pd $3d_{3/2}$ at 334.9 and 340.2 eV, respectively; they are readily assigned to metallic Pd. The results strongly suggest the successful anchoring of zero-valence Pd atoms on the GDY, forming Pd^0/GDY ACs. These features would presumably be beneficial for improving the intrinsic catalytic activity of GDY-based ACs (Xue et al., 2018a, 2018b).

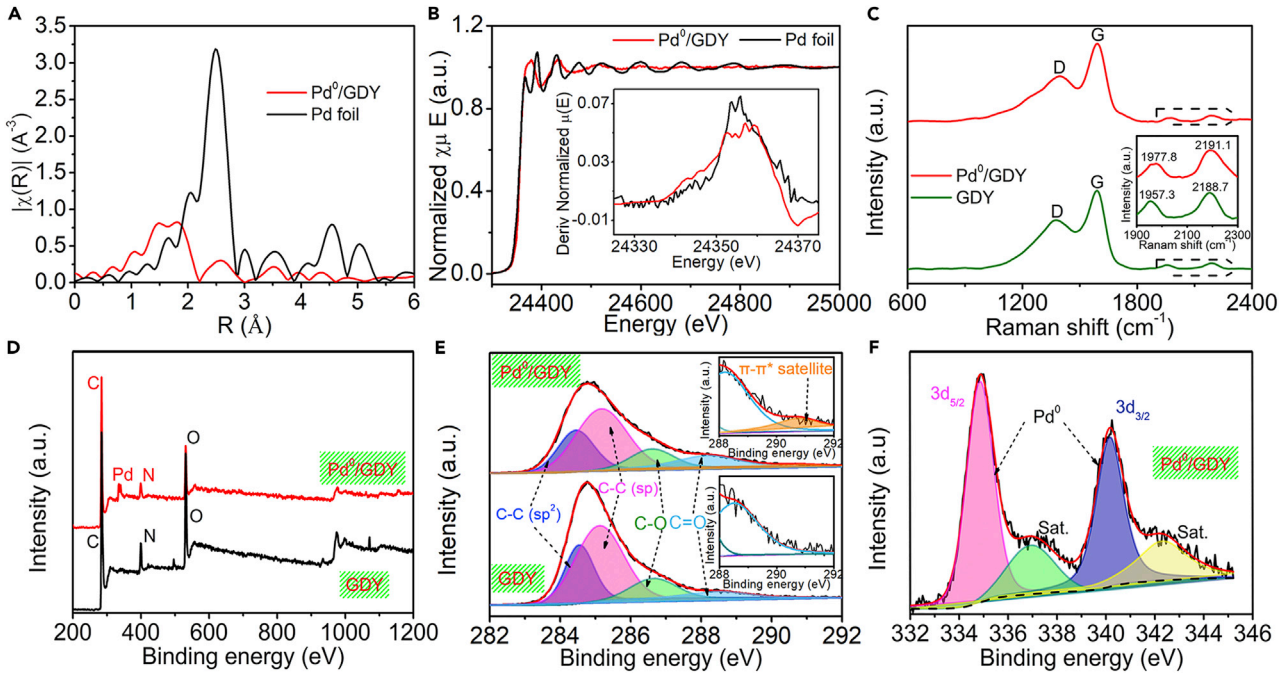

Figure 5. Structural Characterization

(A) EXAFS spectra of Pd^0/GDY and Pd foil at the Pd K-edge.

(B) The normalized Pd K-edge XANES spectra and first-derivative curves (the inset) of Pd^0/GDY and Pd foil.

(C) Raman spectra of Pd^0/GDY and the pristine GDY. Inset: signals for the diyne structure of the GDY skeleton; see also Figure S9.

(D) XPS survey spectra of Pd^0/GDY and the pristine GDY.

(E) High-resolution XPS C 1s spectra of Pd^0/GDY and the pristine GDY (insets are the magnified images of the 290.8-eV region); see also Figure S7.

(F) XPS Pd 3d spectrum of Pd^0/GDY.

Electrochemical Characterization

We evaluated the HER catalytic performance of the Pd^0/GDY sample using a typical three-electrode system in H_2-saturated 0.5 M H_2SO_4 (see Transparent Methods for details; Video S1). The pristine GDY, the bare CF substrate (Figure 6A), a Pd NP-decorated GDY (Pd NP/GDY), and commercial Pt/C (20 wt %) loaded on CF (mass loading: 0.447 mg cm^{-2}) were all tested for comparison. The Pd^0/GDY sample was flexible and could be bent in random directions (Figure 6B)—a potentially beneficial property for its application as a working electrode (Figure 6C). Figure 6D presents the *iR*-corrected linear sweep voltammetry curves of the as-prepared samples. Pd^0/GDY provided an overpotential (η) of 55 mV at a current density of 10 mA cm^{-2}, less than those of 20 wt % Pt/C (62 mV), Pd NP/GDY (115 mV), pure GDY (481 mV), and CF (725 mV). This value compares favorably with those of most recently reported ACs and bulk catalysts, including Pt-MoS_2 (Deng et al., 2015), Pt_1@Fe-N-C (Zeng et al., 2018), and PtO_x/TiO_2 (Cheng et al., 2017) (Figures 6E and Tables S1 and S2). Measurement of the mass activity provided a more straightforward approach toward evaluating the catalytic performance. We obtained the mass activities of Pd^0/GDY and Pt/C normalized in terms of the metal loading (Figure 6F; see also Transparent Methods for details). As expected, the mass activity of Pd^0/GDY was much better than that of Pt/C. For instance, at the overpotential of 0.2 V, Pd^0/GDY presented a specific activity of 61.5 A mg_{metal}^{-1}, which was 26.9 times greater than that of Pt/C (2.29 A mg_{metal}^{-1}). The Tafel slope of a catalyst is an indicative index for understanding the inherent kinetics of the HER process. As displayed in Figure 6G, Pd^0/GDY provided a Tafel slope of 47 mV dec^{-1}, which was lower than those of Pd NP/GDY (139 mV dec^{-1}), the GDY (212 mV dec^{-1}), and the CF (295 mV dec^{-1})—indeed, it was lower than those of most of the reported ACs and state-of-art bulk catalysts (Figures 6H and Tables S1 and S2). This value for the Tafel slope suggests that the HER process of Pd^0/GDY proceeds through a Volmer-Heyrovsky mechanism, in which hydrogen desorption is the rate-determining step. By extrapolating Tafel plots to a value of potential of 0, we obtained the exchange current density (j_0) and used it to assess the HER activity kinetically. The value of j_0 of Pd^0/GDY was 0.282 mA cm^{-2}; it is much higher than those of most previously reported ACs and benchmarked bulk catalysts, including Co-nitrogen-doped graphene (0.125 mA cm^{-2}) (Fei et al., 2015) and Ni_2P@N-doped porous carbon nanofibers

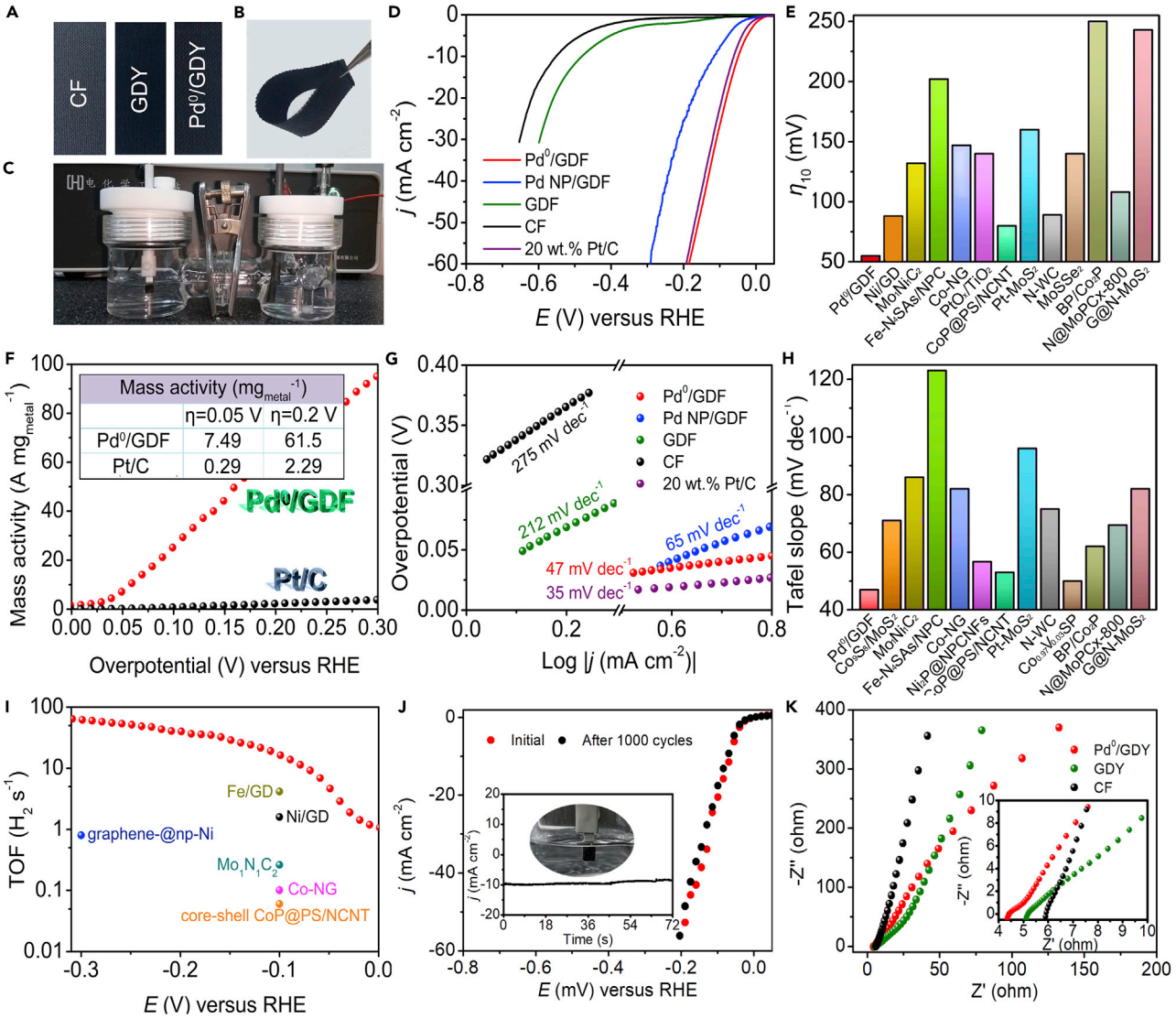

Figure 6. HER Performances

(A) Photographs of Pd^0/GDY, GDY, and CF, which was used as the working electrode for the HER test.

(B) Photograph displaying the flexibility of Pd^0/GDY.

(C) Photograph of the established three-electrode system.

(D) Polarization curves of Pd^0/GDY, Pd NP/GDY, GDY, CF, and Pt/C.

(E) Overpotentials at 10 mA cm^{-2} of other recent ACs and several bulk catalysts; see also Tables S1 and S2.

(F) Mass activity of Pd^0/GDY and Pt/C (inset: mass activity collected at overpotentials of 0.05 and 0.2 V).

(G) Corresponding Tafel slope of the catalysts in (A).

(H) Tafel slopes of other recent ACs and several bulk catalysts; see also Tables S1 and S2.

(I) TOF values of Pd^0/GDY together with those of several recent ACs and bulk catalysts.

(J) Polarization curves of Pd^0/GDY before and after 1,000 cycle tests. Inset: time-dependent current density curve of Pd^0/GDY obtained at −58 mV versus reversible hydrogen electrode (RHE); hydrogen evolution on the Pd^0/GDY electrode; see also Figures S10–S13.

(K) Nyquist plots of the catalysts; see also Figures S14 and S15 and Table S3.

(0.227 mA cm^{-2}) (Wang et al., 2018), suggesting a more rapid HER rate and an additional kinetic advantage for Pd^0/GDY. Moreover, compared with Pd NP/GDY, the HER process of Pd^0/GDY was favorable, confirming that the enhanced atomic efficiency of ACs could effectively boost the catalytic activity even at a lower total Pd atom loading. We ascribe this remarkably enhanced HER catalytic activity to the associated interactions between the GDY substrate and the individual Pd atoms.

Turnover frequency (TOF) is a useful criterion when evaluating the authentic activities of catalysts having various mass loadings (Wang et al., 2018). Considering that the anchored metal atoms in ACs are separated adequately from one another, it is reasonable to assume that all the metal atoms would be exposed to the electrolyte and be catalytically active (see Transparent Methods for details). Each metal atom can be regarded as an active site. In this case, we estimated the number of active sites for Pd^0/GDY to be 5.1×10^{15} cm^{-2}; this value is 3.4 times larger than that of Pt(111) (1.5×10^{15} cm^{-2}) (Kibsgaard et al., 2014). At a value of η of 0.1 V (Figure 6I), we calculated the TOF of Pd^0/GDY to be 16.7 s^{-1}—a value much higher than those of Pt/C (11.5 s^{-1}) (Jaramillo et al., 2007), Pt-GT (7.22 s^{-1}) (Tiwari et al., 2018), and conventional single-atom catalysts, including $Mo_1N_1C_2$ (0.262 s^{-1}) (Chen et al., 2017) and Co-NG (0.101 s^{-1}) (Hu et al., 2017). To further evaluate the performance of Pd^0/GDY for practical applications, we examined its long-term stability. Figure 6J displays the results of continuous cycling tests of the Pd^0/GDY conducted from −0.6 V to +0.2 V over 1,000 cycles. After concluding the cycling test, the polarization curve revealed no variation in current density from that recorded initially. No clusters and particles could be observed on the surface of the catalyst after the stability test, further excluding the possible aggregation of Pd atoms (Figure S10). Scanning electron microscopic images (Figure S10) and XPS data (Figures S11–S13) indicated that Pd^0/GDY maintained its unique morphological and chemical structures over a long period of time, confirming its robust structural stability during the HER process. In addition, a chronoamperometric test performed at a constant overpotential provided almost no decrease in current density over 72 hr, confirming the reliable stability of Pd^0/GDY.

To gain deeper insight into the origin of the high catalytic activity of Pd^0/GDY, we collected electrochemical impedance spectroscopy (EIS) data and fitted it to the R(QR) (QR) equivalent circuit model (Figure S14) containing the uncompensated solution resistance (R_s) and the charge transfer resistance (R_{ct}) (Figures 6K and S15). The fitted parameters are listed in Table S3. Pd^0/GDY exhibited smaller values of R_s (4.55 Ω) and R_{ct} (3.37 Ω) than those of the pristine GDY (R_s = 5.30 Ω; R_{ct} = 30.97 Ω) and CF (R_s = 6.10 Ω; R_{ct} = 54.37 Ω), suggesting that the charge transfer behavior of Pd^0/GDY toward the HER was the most favorable. EIS data can also reveal the actual electrocatalytically active surface area (ECSA) of a catalyst, through calculation of the electrochemical double-layer capacitance (C_{dl}) (McCrory. et al., 2015; see also Transparent Methods for details). The values of C_{dl} for Pd^0/GDY, GDY, and CF were 0.395, 0.137, and 0.0033 mF, respectively. The ECSA for Pd^0/GDY was 11.29 cm^2—that is, it was 2.87 and 112 times larger than those of the pristine GDY (3.91 cm^2) and the CF (0.10 cm^2), respectively, indicating much more electrocatalytically active sites of Pd^0/GDY, which might be the main reason of the improvement of the HER kinetics.

DISCUSSION

We have used GDY as a supporting material to synthesize a novel zero-valent Pd single-atom catalyst. This Pd^0/GDY sample exhibited excellent HER activity with a smaller overpotential at 10 mA cm^{-2}, a better mass activity, and a higher TOF than commercial Pt/C (20 wt %). We attributed this excellent HER activity to the following four factors. (1) The unique and exact chemical and electronic structures of GDY allow the synthesis of ACs with determined structures and valence states (zero valence), guaranteeing reliable HER performance of the catalyst; they also allow us to obtain atomic-level understanding of the catalytic mechanisms and the rational design of new electrocatalysts. (2) The successful anchoring of isolated Pd atoms on the GDY maximized the atomic efficiency and the number of active sites available for the HER. (3) The strong p–d coupling between the Pd atom and the (C1, C2) atoms in the GDY activated the d electrons from the Pd atom onto the (C1, C2) atoms for effective proton-electron charge exchange, leading to a strong energetic preference to adsorb the H atom and lower the reaction energy barrier, ultimately resulting in a near-zero free energy (ΔG) for the HER. (4) The porous nature of Pd^0/GDY favored rapid mass transport and gas evolution and ensured sufficient contact between the electrolyte and the catalyst surfaces. Furthermore, the Pd^0/GDY exhibited long-term stability, which we ascribe to the mechanically and chemically inert nature of GDY and the intimate interactions between the anchored single Pd atoms and the GDY.

Limitations of Study

Our study demonstrates that the yne-rich GDY and its cavity structure can stabilize zero-valent palladium atoms through the associated effects. Compared with conventional electrocatalysts, new insights into the catalytic process and mechanism at the atomic level have been provided theoretically and experimentally. The electrocatalytic performances of Pd^0/GDY ACs are very promising, which are better than that of commercial Pt/C (20 wt %). However, our electrochemical experiments mainly focus on HER in acidic conditions.

Therefore the application of zero-valent metal atom catalysts in other energy conversion and storage process will be necessary to expand the importance of ACs.

METHODS

All methods can be found in the accompanying Transparent Methods supplemental file.

SUPPLEMENTAL INFORMATION

Supplemental Information includes Transparent Methods, 15 figures, 3 tables, and 1 video and can be found with this article online at https://doi.org/10.1016/j.isci.2018.12.006.

ACKNOWLEDGMENTS

This study was supported by the National Nature Science Foundation of China (21790050 and 21790051), the National Key Research and Development Project of China (2016YFA0200104), and the Key Program of the Chinese Academy of Sciences (QYZDY-SSW-SLH015). We thank the XAFS station (beam line 1W1B) of the Beijing Synchrotron Radiation Facility.

AUTHOR CONTRIBUTIONS

Yuliang Li conceived and designed the research and analysis, and reviewed and edited this manuscript. H.Y. carried out the catalyst preparation, characterizations, and electrochemical experiments and wrote the draft of manuscript. Y.X. helped with the analysis of data, the manuscript's organization, and editing of the draft. B.H. performed the theoretical calculations. L.H., C.Z., Y.F., Y. Liu, Y.Z., Yongjun Li, and H.L. gave technical support and helpful advice.

DECLARATION OF INTERESTS

The authors declare no competing interests.

Received: October 17, 2018
Revised: November 16, 2018
Accepted: December 4, 2018
Published: January 25, 2019

REFERENCES

Chen, W., Pei, J., He, C.T., Wan, J., Ren, H., Zhu, Y., Wang, Y., Dong, J., Tian, W.C., Cheong, S., et al. (2017). Rational design of single molybdenum atoms anchored on N-doped carbon for effective hydrogen evolution reaction. Angew.Chem. Int. Ed. *56*, 16086–16090.

Cheng, X., Li, Y., Zheng, L., Yan, Y., Zhang, Y., Chen, G., Sun, S., and Zhang, J. (2017). Highly active, stable oxidized platinum clusters as electrocatalysts for the hydrogen evolution reaction. Energy Environ. Sci. *10*, 2450–2458.

Dai, L., Xue, Y., Qu, L., Choi, H.-J., and Baek, J.-B. (2015). Metal-free catalysts for oxygen reduction reaction. Chem. Rev. *115*, 4823–4892.

Deng, J., Li, H., Xiao, J., Tu, Y., Deng, D., Yang, H., Tian, H., Li, J., Ren, P., and Bao, X. (2015). Triggering the electrocatalytic hydrogen evolution activity of the inert two-dimensional MoS_2 surface via single-atom metal doping. Energy Environ. Sci. *8*, 1594–1601.

Fan, L., Liu, P.F., Yan, X., Gu, L., Yang, Z.Z., Yang, H.G., Qiu, S., and Yao, X. (2016). Atomically isolated nickel species anchored on graphitized carbon for efficient hydrogen evolution electrocatalysis. Nat. Commun. *7*, 10667.

Fei, H., Dong, J., Arellano-Jiménez, M.J., Ye, G., Kim, N.D., Samuel, E.L.G., Peng, Z., Zhu, Z., Qin, F., Bao, J., et al. (2015). Atomic cobalt on nitrogen-doped graphene for hydrogen generation. Nat. Commun. *6*, 8668.

Fei, H., Dong, J., Feng, Y., Allen, C.S., Wan, C., Volosskiy, B., Li, M., Zhao, Z., Wang, Y., Sun, H., et al. (2018). General synthesis and definitive structural identification of $M_1N_4C_4$ single-atom catalysts with tunable electrocatalytic activities. Nat. Catal. *1*, 63–72.

Gao, X., Li, J., Du, R., Zhou, J., Huang, M.-Y., Liu, R., Li, J., Xie, Z., Wu, L.-Z., Liu, Z., and Zhang, J. (2017). Direct synthesis of graphdiyne nanowalls on arbitrary substrates and its application for photoelectrochemical water splitting cell. Adv. Mater. *29*, 1605308.

Goff, A.L., Artero, V., Jousselme, B., Tran, P.D., Guillet, N., Métayé, R., Fihri, A., Palacin, S., and Fontecave, M. (2009). From hydrogenases to noble metal–free catalytic nanomaterials for H_2 production and uptake. Science *326*, 1384–1387.

He, J.J., Ma, S.Y., Zhou, P., Zhang, C.X., He, C.Y., and Sun, L.Z. (2012). Magnetic properties of single transition-metal atom absorbed graphdiyne and graphyne sheet from DFT + U calculations. J. Phys. Chem. C *116*, 26313–26321.

Hu, J., Zhang, C., Jiang, L., Lin, H., An, Y., Zhou, D., Leung, M.K.H., and Yang, S. (2017). Nanohybridization of MoS_2 with layered double hydroxides efficiently synergizes the hydrogen evolution in alkaline media. Joule *1*, 383–393.

Huang, B. (2016a). Intrinsic deep hole trap levels in Cu_2O with self-consistent repulsive Coulomb energy. Solid State Commun. *230*, 49–53.

Huang, B. (2016b). Strong compensation hinders the p-type doping of ZnO: a glance over surface defect levels. Solid State Commun. *237–238*, 34–37.

Huang, B. (2017). The screened pseudo-charge repulsive potential in perturbed orbitals for band calculations by DFT+U. Phys. Chem. Chem. Phys. *19*, 8008–8025.

Huang, B. (2016c). 4f fine-structure levels as the dominant error in the electronic structures of binary lanthanide oxides. J. Comput. Chem. *37*, 825–835.

Huang, C., Li, Y., Wang, N., Xue, Y., Zuo, Z., Liu, H., and Li, Y. (2018). Progress in research into 2D graphdiyne-based materials. Chem. Rev. *118*, 7744–7803.

Jaramillo, T.F., Jørgensen, K.P., Bonde, J., Nielsen, J.H., Horch, S., and Chorkendorff, I. (2007). Identification of active edge sites for electrochemical H_2 evolution from MoS_2 nanocatalysts. Science *317*, 100–102.

Jia, Z., Li, Y., Zuo, Z., Liu, H., Huang, C., and Li, Y. (2017). Synthesis and properties of 2D carbon—graphdiyne. Acc. Chem. Res. *50*, 2470–2478.

Jiao, Y., Zheng, Y., Jaroniec, M., and Qiao, S.Z. (2015). Design of electrocatalysts for oxygen- and hydrogen-involving energy conversion reactions. Chem. Soc. Rev. *44*, 2060–2086.

Jones, J., Xiong, H., DeLaRiva, A.T., Peterson, E.J., Pham, H., Challa, S.R., Qi, G., Oh, S., Wiebenga, M.H., Pereira Hernández, X.I., et al. (2016). Thermally stable single-atom platinum-on-ceria catalysts via atom trapping. Science *353*, 150–154.

Karunadasa, H.I., Montalvo, E., Sun, Y., Majda, M., Long, J.R., and Chang, C.J. (2012). A molecular MoS_2 edge site mimic for catalytic hydrogen generation. Science *335*, 698–702.

Kibsgaard, J., Jaramillo, T.F., and Besenbacher, F. (2014). Building an appropriate active-site motif into a hydrogen-evolution catalyst with thiomolybdate $[Mo_3S_{13}]^{2-}$ clusters. Nat. Chem. *6*, 248–253.

Kolter, M., Bock, K., Karaghiosoff, K., and Koszinowski, K. (2017). Anionic palladium(0) and palladium(II) ate complexes. Angew.Chem. Int. Ed. *56*, 13244–13248.

Li, Y. (2017). Design and self-assembly of advanced functional molecular materials—from low dimension to multi-dimension. Sci. Sin. Chim. *47*, 1045–1056.

Li, G., Li, Y., Liu, H., Guo, Y., Li, Y., and Zhu, D. (2010). Architecture of graphdiyne nanoscale films. Chem. Commun. *46*, 3256–3258.

Li, Y., Xu, L., Liu, H., and Li, Y. (2014a). Graphdiyne and graphyne: from theoretical predictions to practical construction. Chem. Soc. Rev. *43*, 2572–2586.

Li, Z.-Y., Yuan, Z., Li, X.-N., Zhao, Y.-X., and He, S.-G. (2014b). CO oxidation catalyzed by single gold atoms supported on aluminum oxide clusters. J. Am. Chem. Soc. *136*, 14307–14313.

Liu, J., Liu, Y., Liu, N., Han, Y., Zhang, X., Huang, H., Lifshitz, Y., Lee, S.-T., Zhong, J., and Kang, Z. (2015). Metal-free efficient photocatalyst for stable visible water splitting via a two-electron pathway. Science *347*, 970–974.

Liu, Y., Xiao, C., Huang, P., Cheng, M., and Xie, Y. (2018). Regulating the charge and spin ordering of two-dimensional ultrathin solids for electrocatalytic water splitting. Chem *4*, 1263–1283.

Liu, P., Zhao, Y., Qin, R., Mo, S., Chen, G., Gu, L., Chevrier, D.M., Zhang, P., Guo, Q., Zang, D., et al. (2016). Photochemical route for synthesizing atomically dispersed palladium catalysts. Science *352*, 797–800.

Long, M.Q., Tang, L., Wang, D., Li, Y.L., and Shuai, Z.G. (2011). Electronic structure and carrier mobility in graphdiyne sheet and nanoribbons: theoretical predictions. ACS Nano *5*, 2593–2600.

Luo, J., Im, J.-H., Mayer, M.T., Schreier, M., Nazeeruddin, M.K., Park, N.-G., Tilley, S.D., Fan, H.J., and Grätzel, M. (2014). Water photolysis at 12.3% efficiency via perovskite photovoltaics and earth-abundant catalysts. Science *345*, 1593–1596.

Luo, Z., Ouyang, Y., Zhang, H., Xiao, M., Ge, J., Jiang, Z., Wang, J., Tang, D., Cao, X., Liu, C., and Xing, W. (2018). Chemically activating MoS2 via spontaneous atomic palladium interfacial doping towards efficient hydrogen evolution. Nat. Commun. *9*, 2120.

Matsuoka, R., Sakamoto, R., Hoshiko, K., Sasaki, S., Masunaga, H., Nagashio, K., and Nishihara, H. (2017). Crystalline graphdiyne nanosheets produced at a gas/liquid or liquid/liquid interface. J. Am. Chem. Soc. *139*, 3145–3152.

McCrory, C.C.L., Jung, S., Ferrer, I.M., Chatman, S.M., Peters, J.C., and Jaramillo, T.F. (2015). Benchmarking hydrogen evolving reaction and oxygen evolving reaction electrocatalysts for solar water splitting devices. J. Am. Chem. Soc. *137*, 4347–4357.

Nie, L., Xiong, H., Peng, B., Ren, Z., Hernandez, X.I.P., DeLaRiva, A., Wang, M., Engelhard, M.H., Kovarik, L., Datye, A.K., and Wang, Y. (2017). Activation of surface lattice oxygen in single-atom Pt/CeO_2 for low-temperature CO oxidation. Sicence *358*, 1419–1423.

Ortalan, V., Uzun, A., Gates, B.C., and Browning, N.D. (2010). Direct imaging of single metal atoms and clusters in the pores of dealuminated HY zeolite. Nat. Nanotechnol. *5*, 506–510.

Roger, I., Shipman, M.A., and Symes, M.D. (2017). Earth-abundant catalysts for electrochemical and photoelectrochemical water splitting. Nat. Rev. Chem. *1*, 0003.

Thomas, J.M. (2015). Catalysis: Tens of thousands of atoms replaced by one. Nature *525*, 325–326.

Tiwari, J.N., Sultan, S., Myung, C.W., Yoon, T., Li, N., Ha, M., Harzandi, A.M., Park, H.J., Kim, D.Y., Chandrasekaran, S.S., et al. (2018). Multicomponent electrocatalyst with ultralow Pt loading and high hydrogen evolution activity. Nat. Energy *3*, 773–782.

Walter, M.G., Warren, E.L., McKone, J.R., Boettcher, S.W., Mi, Q., Santori, E.A., and Lewis, N.S. (2010). Solar water splitting cells. Chem. Rev. *110*, 6446–6473.

Wang, M.Q., Ye, C., Liu, H., Xu, M., and Bao, S.J. (2018). Nanosized metal phosphides embedded in nitrogen-doped porous carbon nanofibers for enhanced hydrogen evolution at all ph values. Angew.Chem. Int. Ed. *57*, 1963–1967.

Wang, L., Zhang, S., Zhu, Y., Patlolla, A., Shan, J., Yoshida, H., Takeda, S., Frenkel, A.I., and Tao, F. (2013). Catalysis and in situ studies of Rh_1/Co_3O_4 nanorods in reduction of NO with H_2. ACS Catal. *3*, 1011–1019.

Xue, Y., Huang, B., Yi, Y., Guo, Y., Zuo, Z., Li, Y., Jia, Z., Liu, H., and Li, Y. (2018a). Anchoring zero valence single atoms of nickel and iron on graphdiyne for hydrogen evolution. Nat. Commun. *9*, 1460.

Xue, Y., Li, Y., Zhang, J., Liu, Z., and Zhao, Y. (2018b). 2D graphdiyne materials: challenges and opportunities in energy field. Sci. China Chem. *61*, 765–786.

Yang, Y., Luo, M., Zhang, W., Sun, Y., Chen, X., and Guo, S. (2018). Metal surface and interface energy electrocatalysis: fundamentals, performance engineering, and opportunities. Chem *4*, 2054–2083.

Yin, P., Yao, T., Wu, Y., Zheng, L., Lin, Y., Liu, W., Ju, H., Zhu, J., Hong, X., Deng, Z., et al. (2016). Single cobalt atoms with precise N-coordination as superior oxygen reduction reaction catalysts. Angew.Chem. Int. Ed. *55*, 10800–10805.

Yu, H., Xue, Y., Hui, L., Zhang, C., Li, Y., Zuo, Z., Zhao, Y., Li, Z., and Li, Y. (2018). Efficient hydrogen production on 3D flexible heterojunction material. Adv. Mater. *30*, 1707082.

Zeng, X., Shui, J., Liu, X., Liu, Q., Li, Y., Shang, J., Zheng, L., and Yu, R. (2018). Single-atom to single-atom grafting of Pt_1 onto FeN_4 Center: Pt_1@FeNC multifunctional electrocatalyst with significantly enhanced properties. Adv. Energy Mater. *8*, 1701345.

Zheng, H., Zhu, Y., and Shi, Y. (2014). Palladium(0)-catalyzed Heck reaction/C-H activation/amination sequence with diaziridinone: a facile approach to indolines. Angew.Chem. Int. Ed. *53*, 11280–11284.

Zhou, J., Gao, X., Liu, R., Xie, Z., Yang, J., Zhang, S., Zhang, G., Liu, H., Li, Y., Zhang, J., and Liu, Z. (2015). Synthesis of graphdiyne nanowalls using acetylenic coupling reaction. J. Am. Chem. Soc. *137*, 7596–7599.

Zou, X., Huang, X., Goswami, A., Silva, R., Sathe, B.R., Mikmekova, E., and Asefa, T. (2014). Cobalt-embedded nitrogen-rich carbon nanotubes efficiently catalyze hydrogen evolution reaction at all pH values. Angew.Chem. Int. Ed. *53*, 4372–4376.

ISCI, Volume *11*

Supplemental Information

Ultrathin Nanosheet of Graphdiyne-Supported Palladium Atom Catalyst for Efficient Hydrogen Production

Huidi Yu, Yurui Xue, Bolong Huang, Lan Hui, Chao Zhang, Yan Fang, Yuxin Liu, Yingjie Zhao, Yongjun Li, Huibiao Liu, and Yuliang Li

Supplemental Information

Supplemental Figures

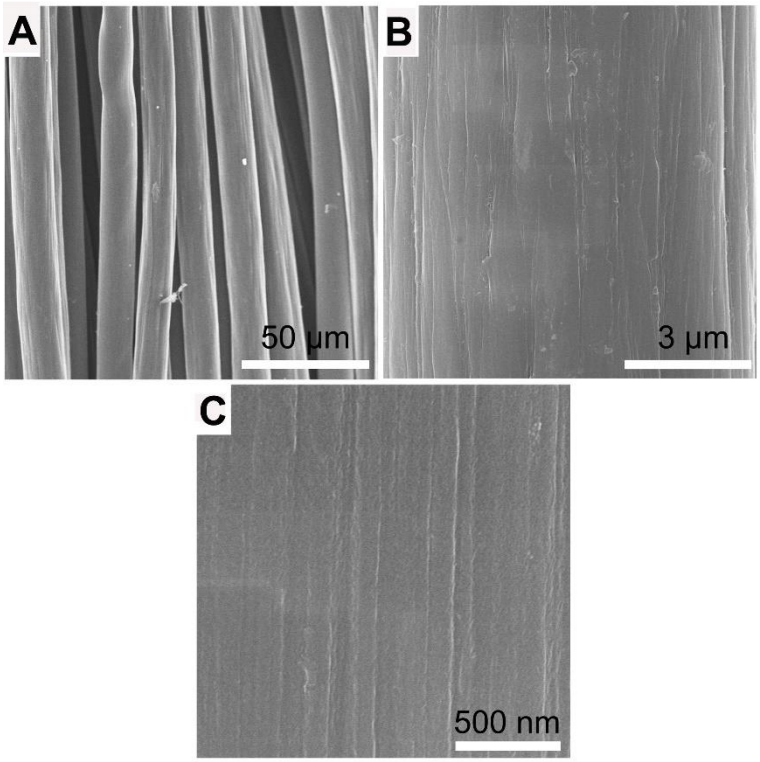

Figure S1. Morphology characterization of CF, related to Figure 3.

(A-C) SEM images of CF in different magnifications. The morphology of smooth CF surface is clearly shown.

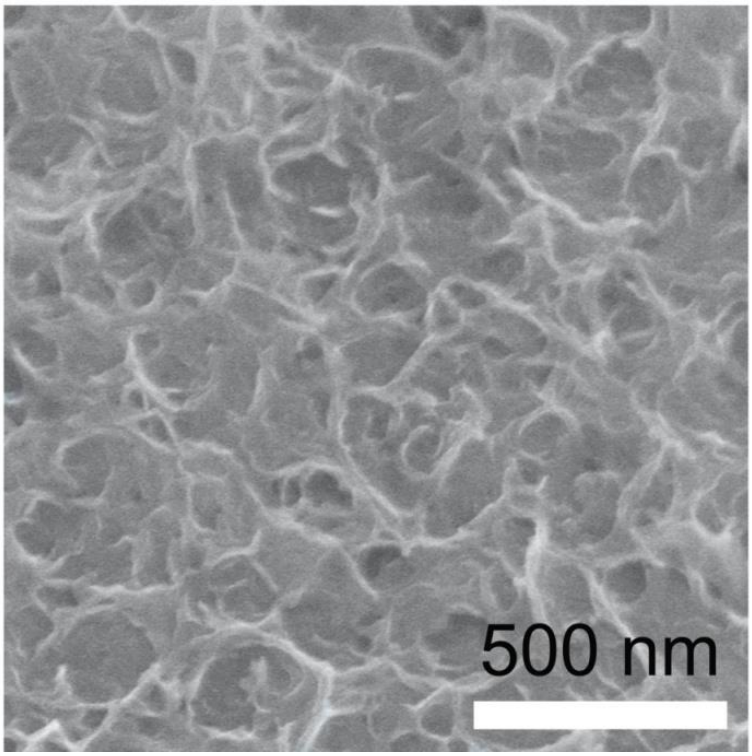

Figure S2. Morphology characterization of GDY, related to Figure 3.

SEM image of pristine GDY.

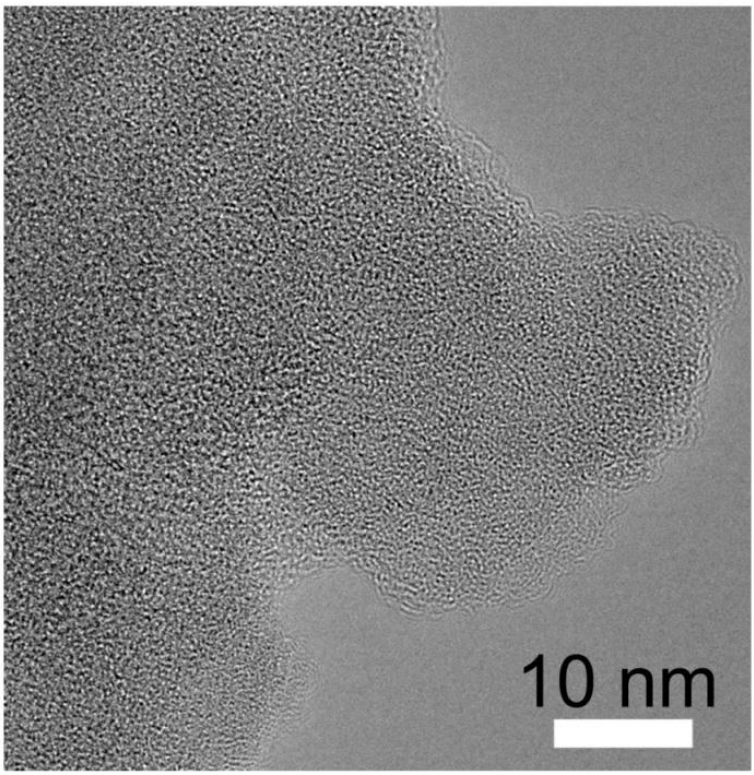

Figure S3. Characterization of GDY, related to Figure 3.

TEM image of the pristine GDY nanosheet.

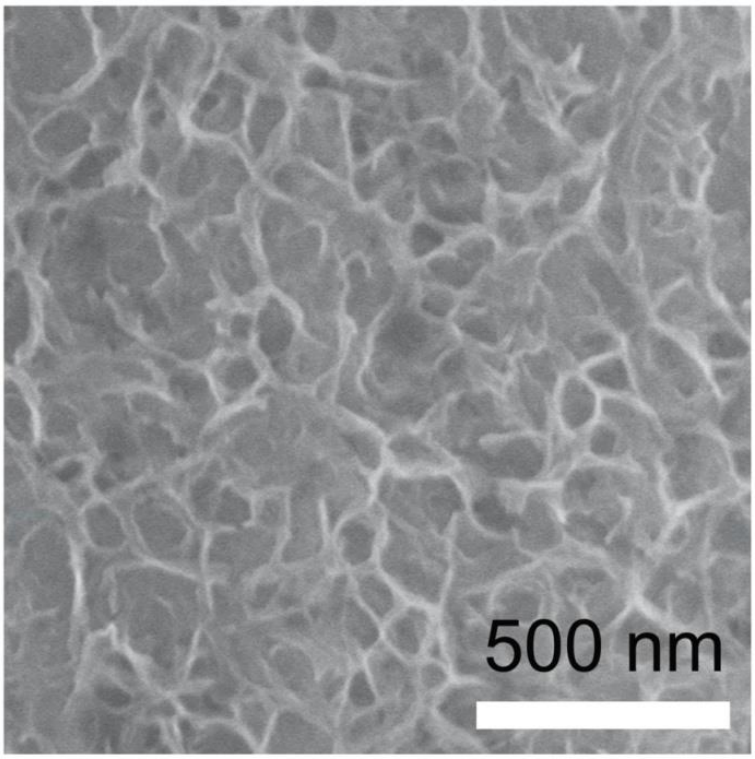

Figure S4. Morphology characterization of Pd^0/GDY, related to Figure 3.

SEM image of Pd^0/GDY, confirming the preservation of nanosheet structure.

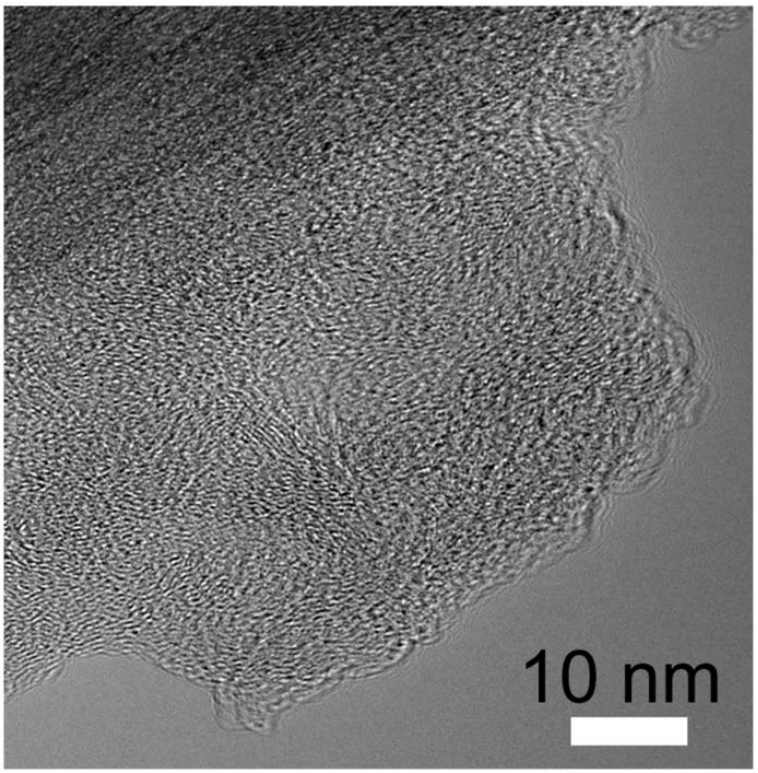

Figure S5. Characterization of Pd^0/GDY, related to Figure 3.

TEM image of Pd^0/GDY, indicating the absence of aggregated Pd nanoparticles.

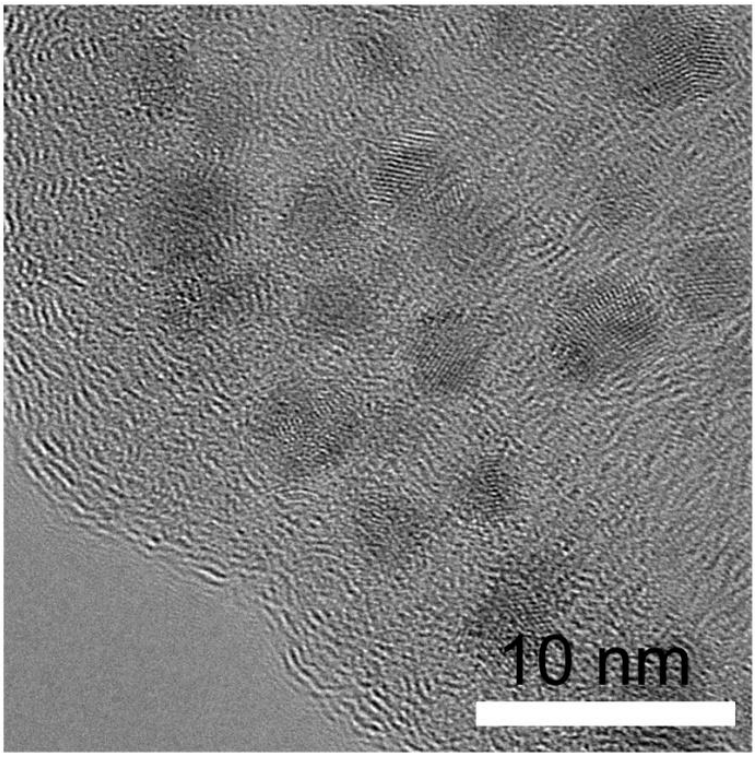

Figure S6. Characterization of Pd NP/GDY, related to Figure 3.

The high-resolution TEM image of Pd NP/GDY, demonstrating the successful deposition of Pd nanoparticles onto GDY substrate.

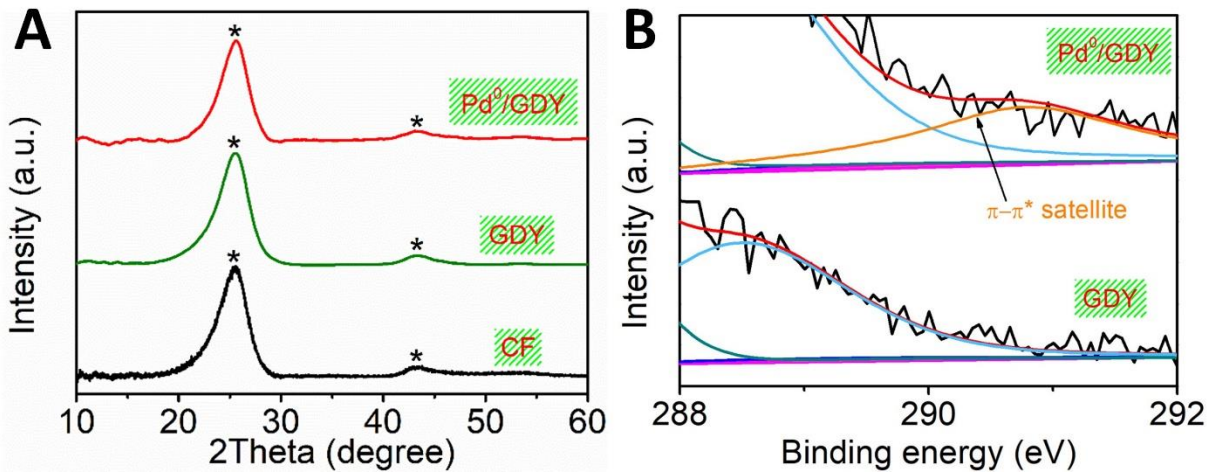

Figure S7. Structural analysis of the as-synthesized samples, related to Figure 5.

(A) XRD patterns of Pd^0/GDY, GDY and CF. The peaks marked with * represent the characteristic peaks of carbon species. No characteristic peaks of Pd species can be observed in Pd^0/GDY. (B) The magnified images of the C 1s at 290.8eV region of Pd^0/GDY and the pristine GDY.

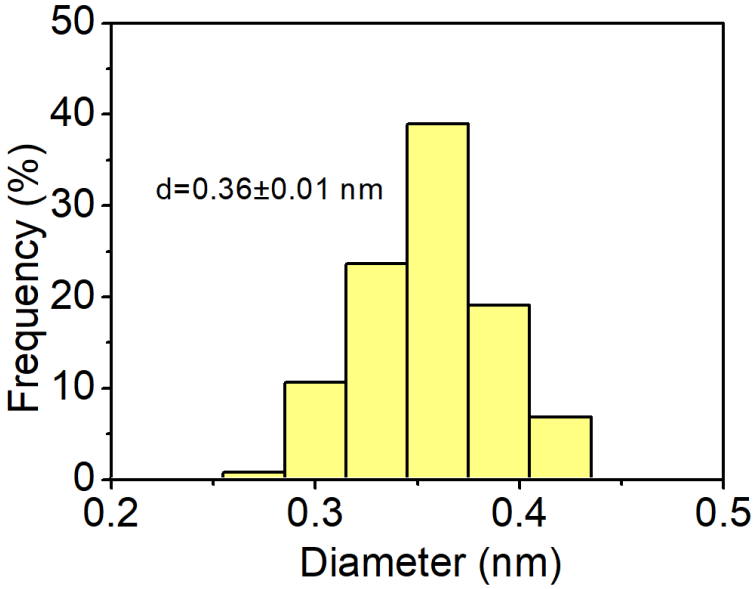

Figure S8. Size distribution, related to Figure 4.

Size distribution of Pd atoms of Pd^0/GDY. The Pd atom size is precisely measured and analyzed from HAADF images of Pd^0/GDY.

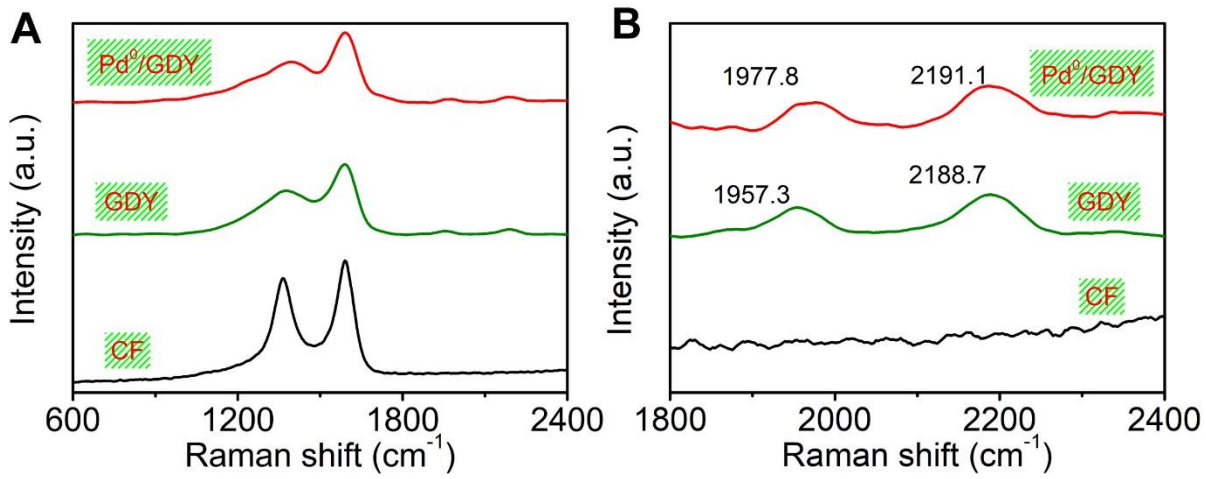

Figure S9. Raman spectra of the catalysts, related to Figure 5.

(A) The Raman spectra of Pd^0/GDY, GDY and CF. (B) The Raman spectra of Pd^0/GDY, GDY and CF within Raman shift from 1800 to 2400 cm^{-1}.

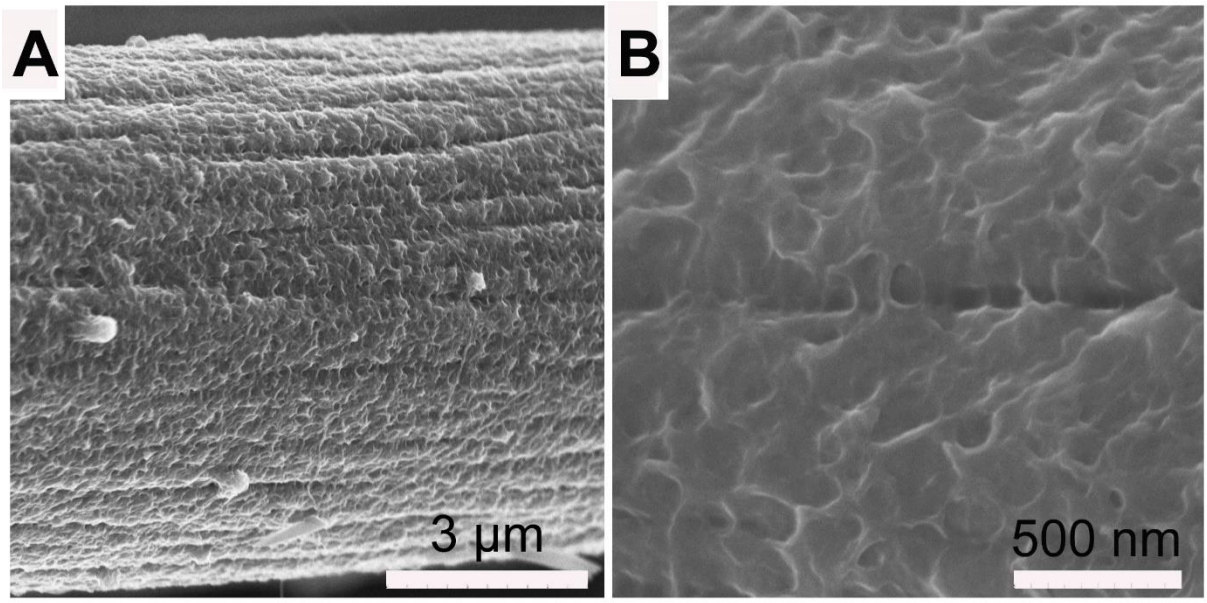

Figure S10. SEM images of Pd^0/GDY after CV cycles, related to Figure 6.

(A) The SEM image of Pd^0/GDY loaded on a single carbon fiber; (B) Magnified image from A.

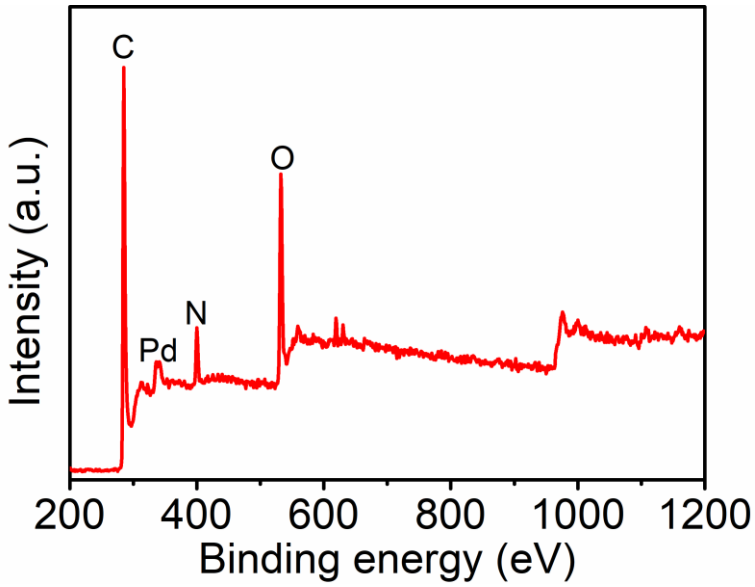

Figure S11. XPS survey spectrum of Pd^0/GDY, related to Figure 6.

XPS survey spectrum of Pd^0/GDY after CV cycles. All the elements remain identical with the sample before CV, indicating the preservation of element composition of Pd^0/GDY.

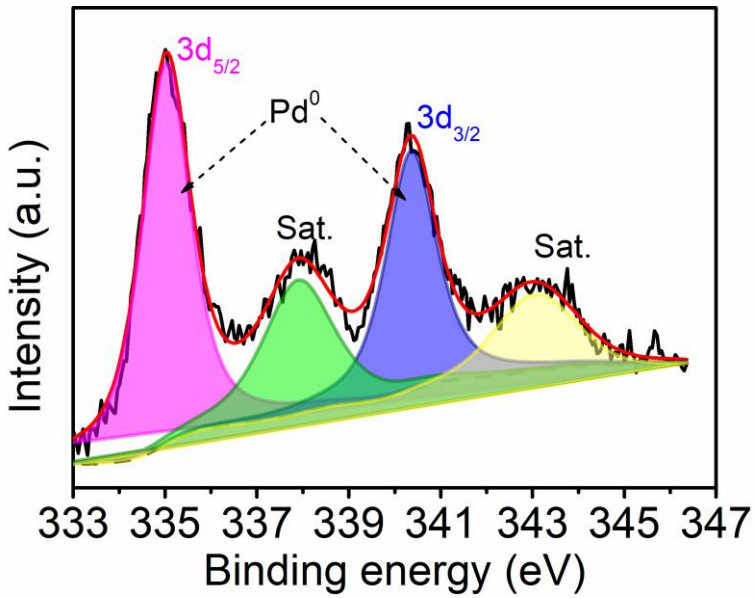

Figure S12. XPS Pd 3d spectrum of Pd^0/GDY after CV cycles, related to Figure 6.

XPS Pd 3d spectrum of Pd^0/GDY after CV cycles. The deconvoluted $3d_{5/2}$ (335.0) and $3d_{3/2}$ (340.4) peaks indicated that Pd remained in its metallic state, confirming the valence reliability of Pd^0/GDY electrocatalyst.

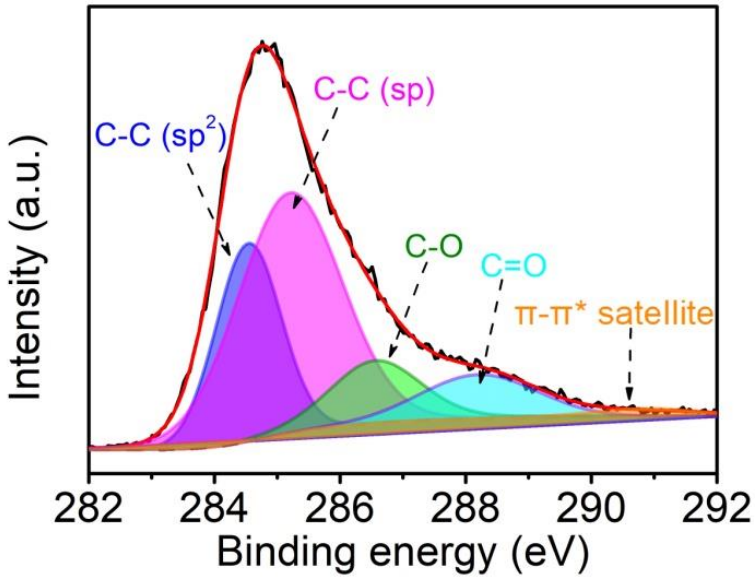

Figure S13. XPS C 1s spectrum of Pd^0/GDY after CV cycles, related to Figure 6.

XPS C 1s spectrum of Pd^0/GDY after CV cycles. Deconvolution indicated the presence of sp-C (285.2 eV), sp^2-C (284.5 eV), C-O (286.6 eV), C=O (288.2 eV) and π-π* transition (290.9 eV), demonstrated the maintained structure and chemical state of GDY network.

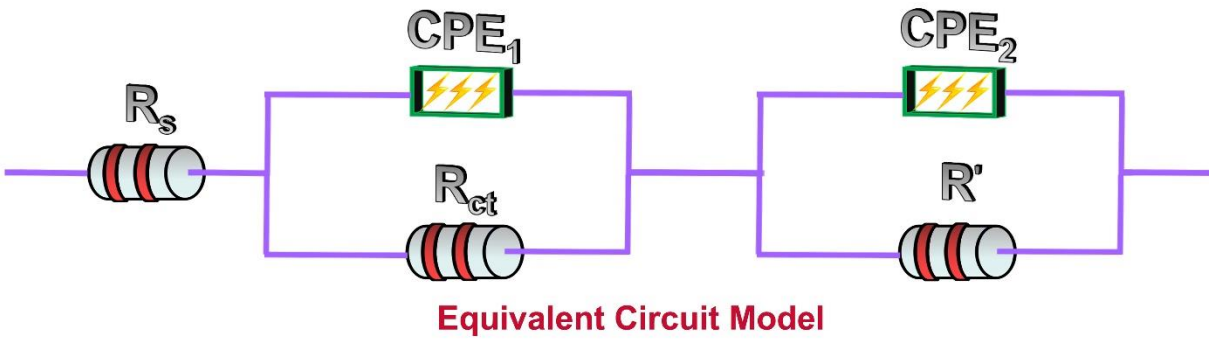

Figure S14. An equivalent circuit model, related to Figure 6.

The R(QR)(QR) equivalent circuit model for fitting and analyzing EIS data.

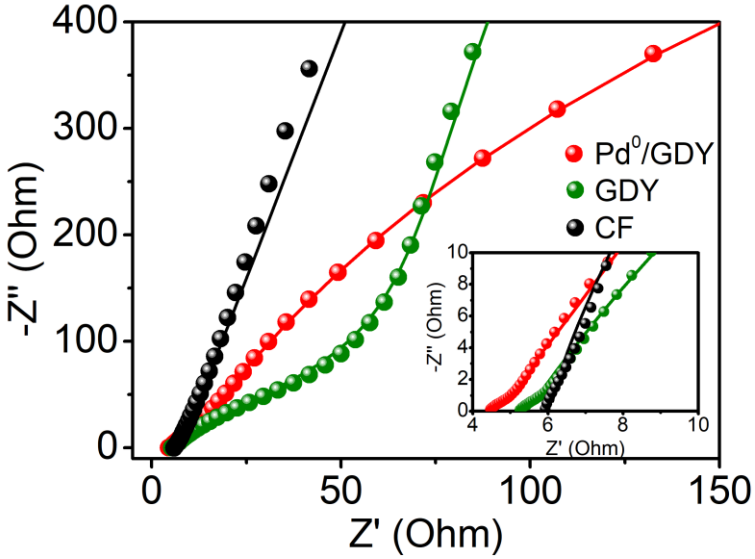

Figure S15. Electrochemical impedance spectroscopy results, related to Figure 6.

The fitted image for EIS data. The spheres represent the experimental Nyquist plots, while the lines with corresponding colors are the fitted results. The inset is the corresponding EIS data in low frequency. The analyzed data fit well with the original experimental EIS data.

Supplemental Tables

Table S1. Comparison of the HER performance of Pd^0/GDY with traditional single-atom catalysts in 0.5 M H_2SO_4, related to **Figure 6**.

Catalysts	**Mass loading (mg cm^{-2})**	**Metal loading**	**η_{onset} (mV)**	**$\eta_{10\ mA\ cm^{-2}}$ (mV)**	**Tafel slope (mV dec^{-1})**	**Stability (cycles)**	**Reference**
Pd^0/GDY	**0.207**	**0.2%**	**11**	**55**	**47**	**1000**	**This work**
$Mo_1N_1C_2$	0.408	1.32%	48	154	86	1000	*Angew. Chem. Int. Ed.* **56,** 16086 (2017)
Co-NG	0.285	0.57%	30	147	82		*Nat. Commun.* **6,** 8668 (2015)
ALDPt/NGNs	N/A	2.1%		ca.60	29	1000	*Nat. Commun.* **7,** 13638 **(**2018**)**
Fe/GD	N/A	0.680%	9	66	37.8	5000	*Nat. Commun.* **9,** 1460 (2018)
Ni/GD	N/A	0.278%		88	45	5000	*Nat. Commun.* **9,** 1460 (2018)
Pt–MoS_2	0.018	1.7%		ca.160	96	5000	*Energy Environ. Sci.* **8,** 1594 (2015)
Co_9S_8/1L MoS_2	N/A	N/A		95	71	1000	*Adv. Mater.* **30,** 1707301 (2018)
Pt1@Fe-N-C	0.4	2.1%		60	42		*Adv. Energy Mater.* **8,** 1701345 (2018)
Fe-N_4 SAs/NPC	N/A	1.96%		202	123		*Angew. Chem. Int. Ed.* **57,** 8614 (2018)

Table S2. Comparison of the HER performances of Pd^0/GDY with benchmarked bulk catalysts in 0.5 M H_2SO_4, related to **Figure 6**.

Catalysts	**Mass loading (mg cm^{-2})**	**η_{onset} (mV)**	**$\eta_{10\ mA\ cm^{-2}}$ (mV)**	**Tafel slope (mV dec^{-1})**	**Stability (cycles)**	**Reference**
Pd^0/GDY	**0.207**	**11**	**55**	**47**	**1000**	**This work**
PtO_x/TiO_2	N/A		ca.140	40	3000	*Energy Environ. Sci.* **10,** 2450 (2017)
$Co_{0.97}V_{0.03}SP$	0.28	23	55	50		*Adv. Energy Mater.* **8,** 1702139 (2018)
core–shell CoP@PS/NCNT	N/A		80	53	1000	*Adv. Energy Mater.* **8,** 1702806 (2018)
N-WC nanoarray	16		89	75		*Nat. Commun.* **9,** 924 (2018)
BP/Co_2P	0.14	105	ca.250	62		*Angew. Chem. Int. Ed.* **57,** 2600 (2018)
N@$MoPC_x$-800	0.14	32	108	69.4	1000	*Adv. Energy Mater.* **8,** 1701601 (2018)
Ni_2P@NPCNFs	N/A	52	63.2	56.7	3000	*Angew. Chem. Int. Ed.* **57,** 1963 (2018)
G@N-MoS_2	0.25		243	82	1000	*Adv. Mater.* **30,** 1705110 (2018)

Table S3. The fitted EIS parameters, related to **Figure 6.**

Catalysts	**R_s (Ω)**	**CPE_1 (S sec^n)**	**n_1**	**R_{ct} (Ω)**	**CPE_2 (S sec^n)**	**n_2**	**R' (Ω)**
Pd^0/GDY	4.549	1.127×10^{-4}	0.9497	3.367	3.623×10^{-4}	0.793	4.422×10^{4}
GDY	5.303	2.175×10^{-4}	0.8213	30.97	1.552×10^{-4}	0.8513	1.508×10^{5}
CF	6.103	3.84×10^{-6}	0.9707	54.37	3.282×10^{-6}	0.8567	1.08×10^{10}

Transparent Methods

Materials

Tetrabutylammonium fluoride (TBAF) was purchased from Alfa Aesar. Hexabromobenzene was brought from J&K Scientific. Toluene and tetrahydrofuran (THF) were refluxed with sodium pieces for sufficient time in order to remove the remaining water. All other reagents were purchased from Sinopharm Chemical Reagent Co., Ltd., and used without further purification unless specifically mentioned. The water used for all experiment was purified with a Millipore system. All the chemicals were of chemical grade and were used as received without further purification.

Preparation of GDY

GDY was synthesized following the previously reported method with minor modification. Several pieces of copper foil and commercial carbon cloth (CC) were added into a three-necked flask containing 100 mL pyridine. The reactor was kept at 110 ^{o}C for 2 hours for the adequate release of catalytic active Cu(I) ions and its sufficient adsorption onto CC. Subsequently, 30 mg HEB was dissolved in 50 mL pyridine and added very slowly into the above flask. The cross-coupling reaction proceeded in the protection of Ar atmosphere at 110 C^{o} in dark. After 3 days, the CC loaded with GDY nanosheet was move out and cleaned with hot acetone and DMF, then thoroughly cleaned with KOH (4 M), HCl (6 M), KOH (4 M) and deionized water in sequence to get rid of the residual copper. The 3D flexible GDY substrate was successfully obtained for the preparation of ACs and subsequent electrochemical tests.

Preparation of Pd^0/GDY

The as prepared GDY substrate was fixed on an electrode clip as working electrode, together with a graphite counter electrode and a saturate calomel reference electrode to establish a three electrode system. The electrochemical deposition was conducted by immersing the GDY electrode into $PdCl_2$ solution (0.2 mM; 0.5 M H_2SO_4 as solvent) and immediately subject to galvanostatic conditions at a current density of 2 mA cm^{-2} for 10 s using an electrochemical workstation (CHI. 660D, Shanghai CH. Instruments, China). The Pd^0/GDY was successfully prepared and washed with H_2SO_4 (0.5 M), deionized water and H_2SO_4 (0.5 M) sequentially, then used for electrochemical measurements immediately. The Pd NP/GDY was synthesized using the electrochemical deposition method. Briefly, the as prepared GDY substrate was used as working electrode, together with a graphite counter electrode and a saturate calomel reference electrode to establish a three electrode system. The GDY electrode was immersed into $PdCl_2$ solution (1.0 mM; 0.5 M H_2SO_4 as solvent) and immediately subject to galvanostatic conditions at a current density of 2 mA cm^{-2} for 100 s. The obtained sample was washed thoroughly using H_2SO_4 (0.5 M) and used for electrochemical measurements immediately.

Calculation setup

We performed the density functional theory (DFT) calculations based on the CASTEP code (Clark et al., 2005). For the electronic orbital potential projection calculations, the related calculations are carried out by recently developed ab-initio orbital self-energy minimization technique (Huang., 2016; Huang., 2016; Huang., 2017; Huang., 2016). This method provides the detail of the self-consistent determination process for the orbital parameters with best matching the specific chemical bonding environment of the given solid materials systems. The on-site electronic orbital negativity induced potential and screened pseudo-charge perturbation induced potential will both be simultaneously projected under the targeted bonding cases. Our related coding technique has been compiled within the simple rotationally invariant DFT+U framework imbedded within the CASTEP source code (Vladimir et al., 1997). The C-2p orbital Hubbard U response is self-consistently performed based on the

Broyden-Fletcher-Goldfarb-Shannon (BFGS) geometry optimization algorithm. The PBE functional is chosen and related plane wave basis set cut-off energy is set at the 750 eV based on a Monkhost-Pack k-point mesh of 4×4×2. The ensemble DFT (EDFT) has been used for improving the electronic minimization to overcome the spurious spin-charge perturbation seen in density-mixing scheme (Marzari et al., 1997). The convergence tolerance of total energy calculation is determined at 5.0 x 10^{-7}eV/atom with ionic force minimization level of 0.001 eV/ Å by Hellmann-Feynman theorem.

The Pd, C, and H norm-conserving pseudopotentials are generated using the OPIUM code in the Kleinman-Bylander projector form (Kleinman et al., 1982), and the non-linear partial core correction for the Pd valence electrons (Louise et al., 1982) and a scalar relativistic averaging scheme (Grinberg et al., 2000) are selected to treat the spin-orbital coupling effect. We chose the (4*d*, 5*s*, 5*p*), (2*s*, 2*p*), (1s) states as the valence states of Pd, C, and H atoms respectively. The RRKJ method is chosen for the optimization of the pseudopotentials (Rappe et al., 1990).The Hubbard U parameters on the Pd-4d orbitals is self-consistently to be U_d=7.56eV.

Characterizations

Scanning electron microscopy (SEM) images were collected using an S-4800 field emission scanning electron microscope. Transmission electron microscopy (TEM), high resolution transmission electron microscopy (HRTEM) and EDX mapping results were carried out on a JEM-2100F electron microscope operating at 200 kV. X-ray diffraction (XRD) was conducted on a Japan Rigaku D/max-2500 rotation anode X-ray diffractometer using Cu Kα radiation (λ = 1.54178 Å). Raman spectra were obtained by e a Renishaw-2000 Raman spectrometer exploiting a 514.5 nm excitation laser source. And a Thermo Scientific ESCALab 250Xi instrument with monochromatic Al Kα X-ray radiation was used to perform the X-ray photoelectron spectroscope (XPS) measurement. Sub-ångström-resolution high-angle annular dark-field (FAADF) scanning transmission electron microscopy (STEM) images were obtained on aberration-corrected cubed FET Titan Cubed Themis G2 300 or JEM-ARM200F (JEOL, Tokyo, Japan) TEM/STEM operated at 200 kV with cold field-emission gun and double hexapole Cs correctors (CEOS GmbH, Heidelberg, Germany).

Electrochemical studies

All electrochemical experiments were performed using an electrochemical workstation (CHI. 660D, Shanghai CH. Instruments, China) with a typical three-electrode system. The as-prepared catalysts were used as working electrode; a graphite rod and saturated calomel electrode (SCE) was employed as the counter electrode and reference electrode, respectively. We used 0.5 M H_2SO_4 (saturated with H_2) as the electrolyte. Linear sweep voltammetry (LSV) measurements were conducted out at a scan rate of 1 mV s^{-1} and cyclic voltammograms (CV) measurements were performed within a range of -0.7 to 0 V at a scan rate of 100 mV s^{-1}. EIS data were gathered a frequency range from 0.1 to 100000 Hz at corresponding open circuit voltage. The chronoamperometric test result was carried out at a constant overpotential to reach an initial current density of 10 mA cm-2. All the potentials acquired were compensated by impedance and calibrated to the reversible hydrogen electrode (RHE).

Calculation of active sites and turn over frequency (TOF)

The TOF value of Pd^0/GDY can be obtained following the equation:

$$\mathrm{TOF} = \frac{\text{total hydrogen tunover per geometrica area}}{\text{active sites per geomtric area}}$$

The total hydrogen turnovers were calculated from the current density given from LSV curves in different overpotential according to the following equation:

total hydrogen tunovers

$$= \left(\mathrm{j}\frac{\mathrm{mA}}{\mathrm{cm}^2}\right)\left(\frac{1\ \mathrm{C/s}}{100\ \mathrm{mA}}\right)\left(\frac{1\ \mathrm{mol\ e^-}}{96485.3\ \mathrm{C}}\right)\left(\frac{1\ \mathrm{mol\ H_2}}{2\ \mathrm{mol\ e^-}}\right)\left(\frac{6.022\times10^{23}\ \mathrm{molecules\ H_2}}{1\ \mathrm{mol\ H_2}}\right)$$

$$= 3.12\times10^{15}\,\frac{\mathrm{H_2/s}}{\mathrm{cm}^2}\,\mathrm{per}\,\frac{\mathrm{mA}}{\mathrm{cm}^2}$$

Since the Pd^0/GDY fulfilled the maximum palladium atom efficiency, it was reasonable to assume that all the individual Pd atoms anchored on GDY could serve as active centers during HER process. Thus the active site can be calculated according to the ICP-MS result:

$$\text{active sites (Pd)} = \left(\frac{\text{mass loading (Pd)} \times \text{catalystloading per geometric area (g/cm}^2)}{\text{Pd Mw (g/mol)}}\right)\left(\frac{6.022\times10^{23}}{1\ \text{mol Pd}}\right)$$

$$= \left(\frac{0.2\%\times0.45\times10^{-3}(\mathrm{g/cm^2})}{106.42\ (\mathrm{g/mol})}\right)\left(\frac{6.022\times10^{23}}{1\ \text{mol Pd}}\right) = 5.1\times10^{15}\ \text{sites per cm}^2$$

The current density was obtained from LSV curve. Therefore, the TOF value was calculated according to the following equation:

$$\mathrm{TOF}_{\mathrm{Pd^0/GDY}} = \left(\frac{3.12\times10^{15}}{5.1\times10^{15}}\times j\right) = 0.612\times j$$

Calculation of mass loading

The mass activity can be calculated according to the equation:

$$\mathrm{j_{mass}} = \frac{\mathrm{j_{geometrical}}}{\mathrm{M_{loading}}}$$

in which $j_{\mathrm{geometrical}}$ is the geometrical current density directly obtained from LSV curve, while $\mathrm{M_{loading}}$ is the catalytically active Pd loading per geometric area calculated form ICP-MS result.

Calculation of double layer capacitance (C_{dl}) and electrochemical active surface area (ECSA)

The C_{dl} values are obtained based on the collected EIS data according to the following equation:

$$C_{dl} = \left[\frac{\mathrm{Q'}}{\left({R_S}^{-1} + {R'}^{-1}\right)^{1-n}}\right]^{(1/n)}$$

Where Rs is the uncompensated solution resistance; R' is the catalytic charge transfer resistance and Q' represents the influence of double layer capacitance. All these impendence parameters are listed in Table S2.

The ECSA values are collected from C_{dl} according to the equation:

$$\mathrm{ECSA} = \frac{C_{dl}}{C_s}$$

The specific capacitance (Cs) of the catalysts is generally considered to be 0.035 mF cm^{-2} in acidic working media according to peer recognition in reported studies.

Supplemental References

Clark, S. J., Segall, M. D., Pickard, C. J., Hasnip, P. J., Probert, M. I., Refson, K., and Payne, M. C. (2005). First principles methods using CASTEP. *Zeitschrift Fur* Kristallographie *220*, 567–570.

Grinberg, I., Ramer, N. J. and Rappe, A. M. (2000). Transferable relativistic dirac-slater pseudopotentials. Phys. Rev. B *62*, 2311.

Huang, B. (2016). Intrinsic deep hole trap levels in Cu_2O with self-consistent repulsive Coulomb energy. Solid State Commun. *230*, 49–53.

Huang B. (2016). Strong compensation hinders the p-type doping of ZnO: a glance over surface defect levels. Solid State Commun. *237*, 34–37.

Huang, B. (2017). The screened pseudo-charge repulsive potential in perturbed orbitals for band calculations by DFT+ U. *Phys.* Chem. Chem. Phys. *19*, 8008–8825.

Huang, B. (2016). 4f fine–structure levels as the dominant error in the electronic structures of binary lanthanide oxides. J. Comput. Chem. *37*, 825–835.

Kleinman, L. and Bylander, D. M. (1982). Efficacious form for model pseudopotentials. Phys. Rev. Lett. *48*, 1425.

Louie, S. G., Froyen, S. and Cohen, M. L. (1982). Nonlinear ionic pseudopotentials in spin-density-functional calculations. Phys. Rev. B *26*, 1738.

Marzari, N., Vanderbilt, D. and Payne, M. C. (1997). Ensemble density-functional theory for ab initio molecular dynamics of metals and finite-temperature insulators. Phys. Rev. Lett. *79*, 1337.

Rappe, A. M., Rabe, K. M., Kaxiras, E. and Joannopoulos, J. D. (1990). Optimized pseudopotentials. Phys. Rev. B *41*, 1227–1230.

Vladimir, I. A., Aryasetiawan, F. and Lichtenstein, A. I. (1997). First-principles calculations of the electronic structure and spectra of strongly correlated systems: the LDA+U method. J. Phys. Condens. Matter. *9*, 767–808.